Probing Dirac Fermions in Graphene by Scanning Tunneling Probes

Adina Luican-Mayer and Eva Y. Andrei

Department of Physics and Astronomy, Rutgers University, Piscataway, NJ 08854, USA

Abstract

Graphene is a two dimensional system which can be studied using surface probe techniques such as scanning tunneling microscopy and spectroscopy. Combining the two, one can learn about the surface morphology as well as about its electronic properties. In this chapter we present a brief review of experimental results obtained on graphene supported on substrates with varying degrees of disorder. In the first part we focus on the electronic properties of single layer graphene without a magnetic field as well as in the presence of a perpendicular magnetic field. The second part focuses on twisted graphene stacks and the effects of rotating away from the equilibrium Bernal stacking on the electronic properties.

Contents

1   Scanning tunneling microscopy and spectroscopy

Scanning tunneling microscopy (STM) is a powerful technique used to study the surface morphology of materials as well as to learn about their electronic properties. The idea behind

the operation of an STM, for which Gerd Binnig and Heinrich Rohrer were awarded the Nobel prize in 1986 [1], is conceptually simple. By bringing a sharp metallic tip atomically close ($\approx$ 1nm) to a conducting sample surface one can create a tunneling junction and when a bias voltage is applied between the two, a tunneling current will start flowing. Such a tunneling junction is depicted in Figure 1. In this situation the electrons below the Fermi level of the sample will be tunneling into the tip, and therefore probe the filled electronic states. In the reverse situation when the Fermi level of the tip is above that of the sample, the electrons are flowing out of the tip into the sample probing the empty states of the sample. The current between the sample and the tip I_t can be calculated from a Fermi Golden rule expression which, assuming low temperatures, can be simplified to [2, 3]:

$$I \propto \frac{4\pi e}{\hbar} \int_0^{eV_{Bias}} \rho_{sample}(\epsilon)\rho_{tip}(eV_{Bias} - \epsilon) \left|M\right|^2 d\epsilon \tag{1}$$

The matrix element, assumed to be constant for the energy interval of integration , $\left|M\right|^2 \propto e^{\frac{-2d}{\hbar}\sqrt{2m\Phi}}$, yields:

$$I \propto e^{\frac{-2s}{\hbar}\sqrt{2m\Phi}} \int_0^{eV_{Bias}} \rho_{sample}(\epsilon)\rho_{tip}(eV_{Bias} - \epsilon)d\epsilon \tag{2}$$

Here ρ_{sample} and ρ_{tip} are the density of electronic states for the sample and tip, d is the separation between the tip and sample, m, e are the electron mass, charge, and Φ is the barrier height.

Topography. Using the STM to measure the topography of a sample is based on the condition that I_t is very sensitive to the tip-sample separation:

$$I \propto e^{\frac{-2d}{\hbar}\sqrt{2m\Phi}} \tag{3}$$

A common measurement mode of STM is the constant current mode in which the tip moves across the sample and it is raised or lowered by a feedback loop in order to keep the tunneling current constant. Tracing the contour made by the tip will give information about the sample topography.

Spectroscopy. If we assume that the tip density of states (DOS) is flat in the energy range of choice, by taking the derivative of I_t with respect to the V_{Bias}, we obtain:

$$\frac{dI_t}{dV_{Bias}} \propto \rho_{sample}(eV) \tag{4}$$

Therefore, the STM can be used to learn about the density of states of the sample in the scanning tunneling spectroscopy (STS) mode. For this, first the junction is set, then the feedback loop is disabled and the tunneling current is recorded while varying the bias voltage. Typically this differential conductance is measured with a lock-in technique by applying a small ac. modulation to the bias voltage. By repeating such a measurement on a grid of points across a chosen region one obtains dI_t/dV_{Bias} maps which reflect the local density of states as a function of spatial coordinates.

In a realistic situation the measurement temperature imposes a lower bound on the resolution which cannot be better than the thermal broadening: E$\approx kT$. For measurements at 4K the minimum resolution is thus $\approx 0.35meV$. At the same time the ac. bias modulation should be comparable to this value for optimal resolution. Furthermore, common materials used for the tip such as Pt/Ir, W, Au typically satisfy the condition of a flat DOS for small
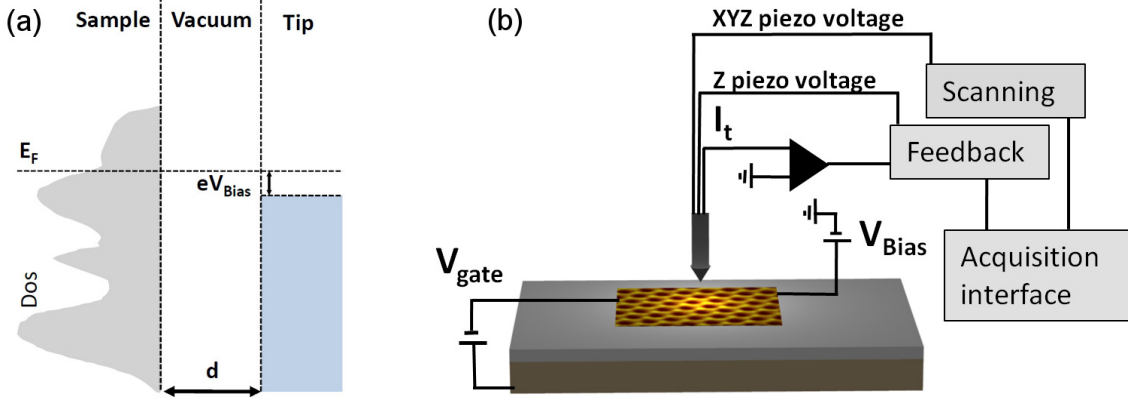
Figure 1: (a) Sketch of the tunneling junction between the tip and the sample in an STM experiment. The important quantities are indicated: the tip-sample separation d, the Fermi level E_F, the bias voltage V_{Bias}. The indicated DOS for the sample has an arbitrary shape and for the tip it is assumed constant.(b) Sketch of the STM set-up in which a graphene flake is placed on a Si/SiO_2 substrate. The main parts of an STM experiment are indicated: the scanning head, the feedback system, the data acquisition interface, the bias voltage and tunneling current. In addition, a gate voltage is applied between the graphene and the gate electrode (typically Si).

enough voltages. For a reliable STS measurement one needs to check that the experiment is done in the vacuum tunneling regime when the dependence of the tunneling current on tip-sample distance is exponential [4]. Reliable spectra are checked to be reproducible as a function of time and they do not depend on the tip-sample distance.

In the following sections we will discuss the results obtained by investigating graphene samples using scanning tunneling microscopy and spectroscopy.

2 From disordered graphene to ideal graphene

Graphene on SiO_2. Graphene was initially isolated by mechanical exfoliation from graphite (Highly Oriented Pyrolitic Graphite (HOPG) or natural graphite) onto Si wafers capped with SiO_2 [5]. In order to fabricate devices from these flakes, metallic contacts are added using standard e-beam lithography. This sample configuration allows using the highly doped Si as a back gate so that by applying a voltage between the flake and the back gate one can tune the carrier density in graphene. Much of the experimental work and in particular transport experiments have used this type of sample, but they are far from ideal.

Firstly, the nanofarbrication procedure can result in disorder that can reside either between the graphene and the SiO_2 or on the surface of graphene. Secondly, graphene will conform to the surface of SiO_2 and it will therefore be rippled. An illustration of this situation is presented in Figure 2. As a consequence of the disorder, the Fermi level of neutral graphene will not coincide with the Dirac point, meaning graphene is doped [6, 7]. The doping varies on the surface of graphene creating puddles of different carrier density (electron-hole puddles)[6, 7].

One of the main sources of the electron-hole puddles in graphene is the random potential induced by the substrate. For the standard SiO_2 substrates which are routinely used in graphene devices this is particularly problematic due to the presence of trapped charges and dangling bonds [8]. Recent experiments demonstrated that the use of dry-chlorinated SiO_2 substrates leads to a significant reduction in the random potential. The use of these substrates

3

gave access to the intrinsic properties of graphene allowing the observation of Landau levels as detailed in a later section [9] (2.4).

Graphene on hexagonal boron nitride (BN), mica etc. More recently, experimental methods were developed to manipulate other 2D materials from layered structures (e.g. BN)[5, 10]. In order to minimize the disorder due to the underlying substrate while still preserving the possibility of gating, graphene was placed on thin flakes of BN which in turn, were previously exfoliated on Si/SiO_2. The quality improvement by using BN as a substrate was significant; the mobilities for devices were above 100000 cm^2/Vs which is an order of magnitude higher than typical graphene devices on SiO_2 [10]. In very high magnetic fields the fractional quantum hall effect was also observed in such samples [11]. Another substrate demonstrated to be suitable for obtaining flat graphene is mica [12].

Graphene flakes on graphite. After cleavage of a graphite crystal, one often finds graphene flakes on the surface which are decoupled from the bulk graphite underneath. These flakes provide the most favorable conditions for accessing the intrinsic electronic properties of graphene as detailed in the following sections [13, 14, 15].

Epitaxial graphene, graphene obtained by chemical vapor deposition etc. Other avenues of producing graphene are epitaxial growth on SiC crystals [16, 17, 18] and chemical vapor deposition (CVD) [19, 20, 21]. In the epitaxial growth one starts with a SiC crystal terminated in Si or C and annealing to temperatures above 1500 ^oC leads to the formation of graphene layers at the surface. Often the layers are misoriented with respect to each other thereby forming Moiré patterns. For the CVD growth, a metallic substrate that plays the role of a catalyst is placed in a hot furnace in a flow of gaseous carbon source. As a result, carbon is absorbed into the metal surfaces at high temperatures and precipitated out to form graphene during cool down to room temperature [22]. Other metallic substrates used for growing graphene films include Ru [23, 24], Ir [25, 26] and Pt [27].

2.1 Surface topography of graphene

The discussion about the morphology of a graphene surface is important because the stability of a 2D membrane in a 3D world is closely related to the tendency toward crumpling or rippling [28, 29]. The degree of rippling also influences the quality of the electronic properties [30]. The morphology of the graphene surface depends strongly on the type of substrate (or lack of substrate) underneath.

Transmission Electron Microscope (TEM) experiments performed on graphene films placed on TEM grids show that there is an intrinsic rippling of the suspended graphene membrane with deformations of up to 1nm [31]. However, when deposited on a flat surface such as mica [12], BN [32, 33], or HOPG [34] the height corrugations become as small as 20-30pm. On the surface of SiO_2 the Van der Waals forces will make graphene conform to the rough surface and typical values reported for the corrugations are 0.5nm in height and a few nm in the lateral dimension [7, 9, 13, 35, 36].

The first STM experiments on graphene deposited on SiO_2 showed that the lattice is indeed hexagonal with almost no defects [37]. Moreover, they also showed the importance of sample cleaning in order to access the pristine graphene surface [38]. A more extensive analysis of the correlation between the substrate roughness and intrinsic graphene roughness [13] suggested that in areas where the graphene does not conform to the oxide surface and it is suspended over the high points, one can find an additional intrinsic corrugation on smaller length scales consistent with TEM studies [31].
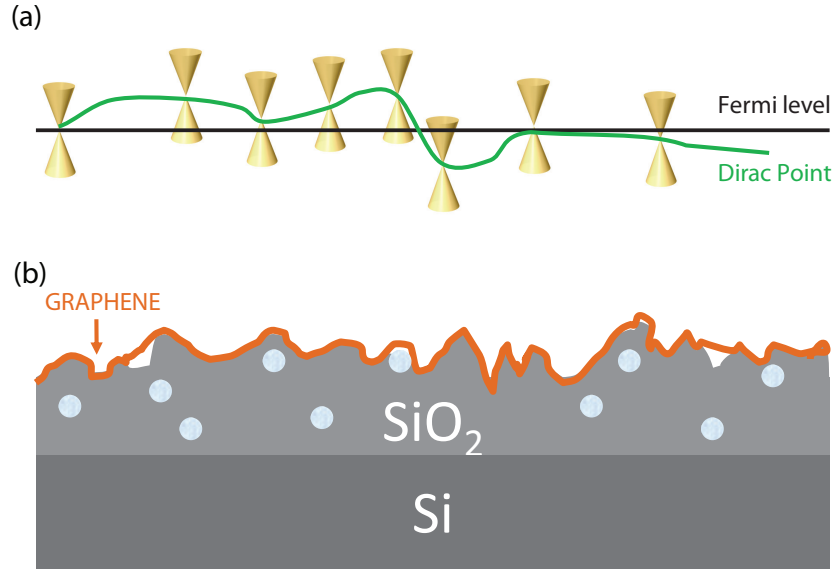
Figure 2: (a) Illustration of the varying carrier concentration across a graphene sample due to the random potential underneath. The Fermi level and the Dirac point are shown by the black and green lines, respectively. (b) Sketch of how graphene (the orange line) deposited on the surface of SiO_2 will have a roughness comparable to the substrate [13]. The light gray dots schematically illustrate trapped charges.

A comparison between typical STM data for graphene on SiO_2 and decoupled graphene flakes on HOPG is presented in Figure 3. In Figure 3(a) the topography of a graphene area on SiO_2 shows a rippled surface. In contrast, graphene on HOPG is much flatter as seen in the topography map in Figure 3(b). The corresponding atomic resolution data demonstrates that despite the corrugation of the surface of graphene, the honeycomb lattice is continuous across the hills and valleys (Figure 3 (c),(d)). Remarkably, in both cases the graphene lattice is defect-free over areas as large as hundreds of nanometers.

When deposited on BN, graphene is significantly flatter than on SiO_2 as shown in Figure 4. A comparison between the surface morphology for areas of graphene on SiO_2 and on BN is presented in Figure 4(a) and (b). Two line cuts arbitrarily shifted in the z direction in Figure 4(c) show that, when placed on BN, graphene is one order of magnitude smoother than on SiO_2. On such samples STM/STS experiments report Moiré patterns that arise because of the lattice mismatch and rotation between graphene and the BN [32, 33]. Furthermore, the random potential fluctuation measured by scanning tunneling spectroscopy appears much smaller than on graphene samples exfoliated on SiO_2 [32, 33].

2.2 Tunneling spectroscopy of graphene

One of the reasons why graphene has attracted so much interest is its unique electronic band structure. In the low energy regime the charge carriers obey a Dirac-Weyl Hamiltonian and have a conical dispersion. To the first approximation, it is possible to obtain a closed analytical form for the density of states at low energy [39]:

$$\rho(E) = \frac{2A_c}{\pi} \frac{|E|}{v_F^2} \tag{5}$$

5
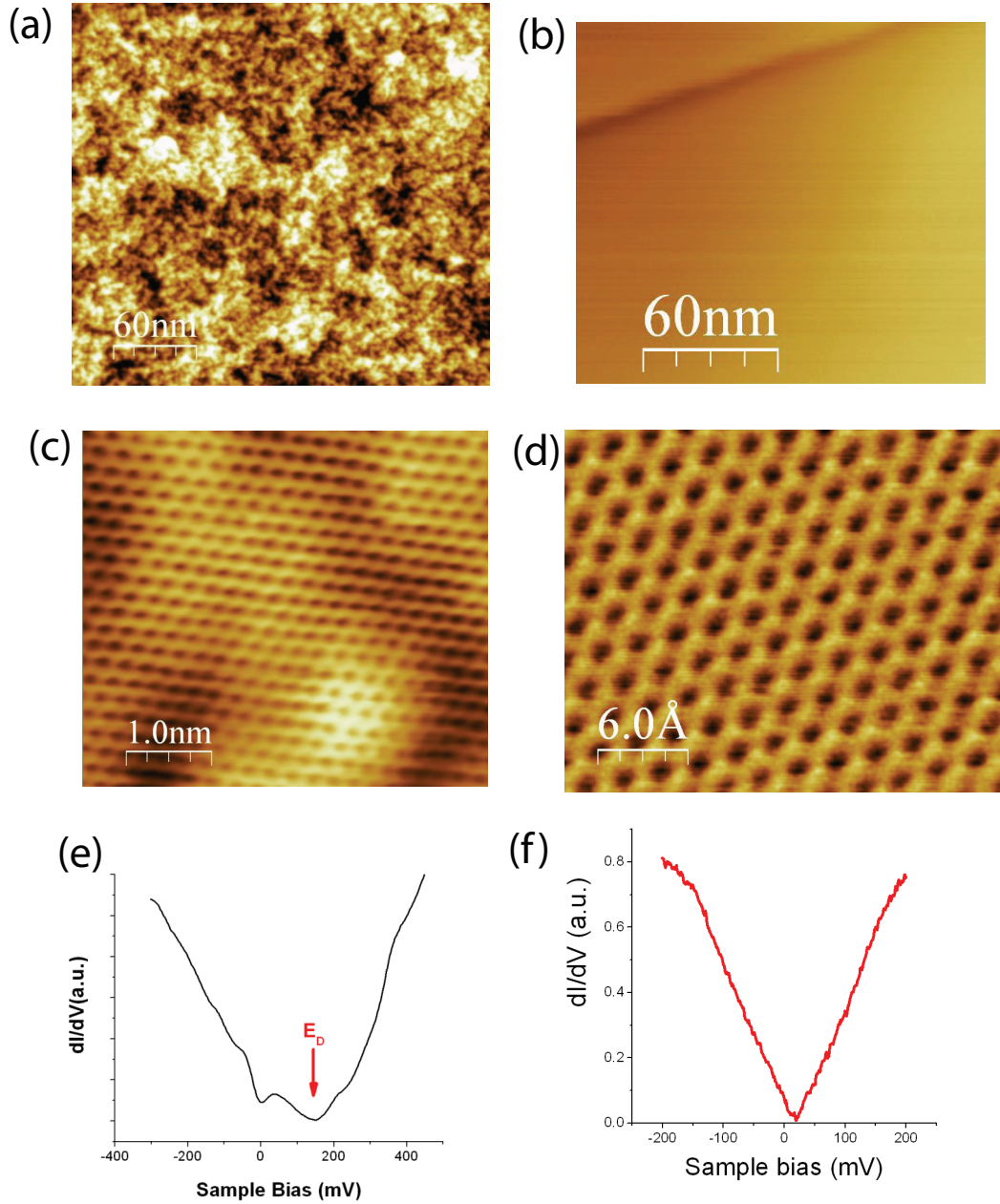
Figure 3: (a) Scanning Tunneling Microscopy image of 300nm x 300nm graphene on a SiO_2 surface (V_{bias}=300mV, I_t=20pA). (b) Scanning Tunneling Microscopy image of 300nmx300nm graphene on graphite surface (V_{bias}=300mV, I_t=20pA). (c),(d) Smaller size image showing atomic resolution on graphene in area (a) and (b), respectively. (e),(f) Scanning Tunneling Spectroscopy data obtained on the corresponding graphene samples in (c) and (d), respectively [9, 34].
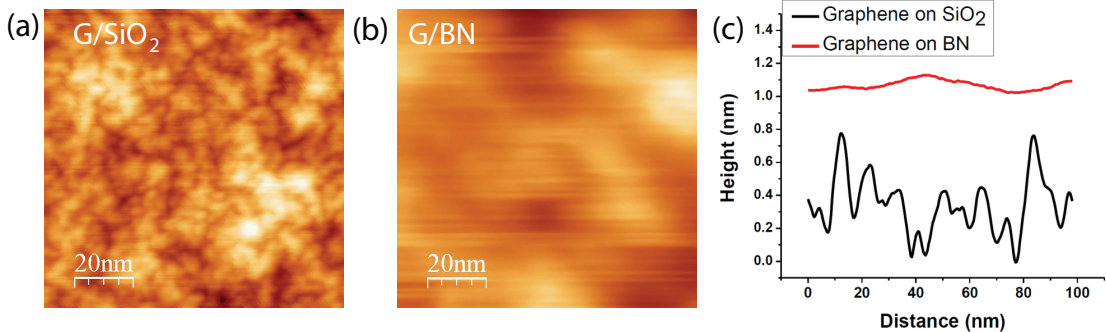
Figure 4: Comparison between the topography of two areas 100nm x 100nm of (a) graphene on SiO_2 and (b) graphene on BN . (c) Comparison between two line cuts across (a),(b).

where, A_c is the unit cell area of graphene lattice.

The DOS in graphene differs qualitatively from that in non-relativistic 2D electron systems leading to important experimental consequences. It is linear in energy, electron-hole symmetric and vanishes at the Dirac point (DP) - as opposed to a constant value in the non-relativistic case. This makes it easy to dope graphene with an externally applied gate voltage. At zero doping, the lower half of the band is filled exactly up to the Dirac points. Applying a voltage to the graphene relative to the gate electrode (when graphene is on Si/SiO_2, the highly doped Si is the back gate) induces a nonzero charge. This is equivalent to injecting, depending on the sign of the voltage, electrons in the upper half of Dirac cones or holes in the lower half. Due to electron-hole symmetry the gating is ambipolar [40].

For graphene on graphite the measured density of states is linear and vanishes at the Dirac point (Figure 3(f)) as expected from theory. For the data shown in Figure 3(f), the Fermi level is slightly shifted away from the Dirac point ($\approx$ 16meV) corresponding to hole doping with a surface density $n = 2 \times 10^{10} cm^{-2}$.

However, when disorder introduces a random potential, as is the case for the graphene on SiO_2, the spectrum deviates from the ideal V-shape [35, 36, 41, 42, 43]. Some of the measured features in the spectra were attributed to strain and ripples [43], others to local doping due to impurities. A typical spectrum is presented in Figure 3(e)[9]. In this case, the Dirac point is shifted from the Fermi energy by $\approx 200 meV$ corresponding to a carrier concentration $n = 2 \times 10^{12} cm^{-2}$.

Some STM experiments on graphene exfoliated on SiO_2 reported a gap at the Fermi level which was attributed to inelastic tunneling into graphene (via phonon scattering) [42]. In other experiments though, the gap is seen only above certain tunneling currents [41]. In most cases a dip at the Fermi level is observed in the tunneling spectra of graphene on SiO_2 [9, 36] which can be attributed to a zero bias anomaly.

2.3 Doping and electron hole puddles

Theoretically, in neutral graphene the Fermi level should coincide with the Dirac point. However, it is observed that graphene is often doped such that there is an energy difference between the Dirac point energy (E_D) and the Fermi energy (E_F). To find the dopant

concentration, the carrier density can be calculated as follows:

$$n = \frac{N}{A} = 4\frac{\pi k_F^2}{(2\pi)^2} = \frac{k_F^2}{\pi} = \frac{1}{\pi}\frac{E_F^2}{\hbar^2 v_F^2} \tag{6}$$

Here the Fermi velocity is $v_F = 10^6 m/s$ and taking $E_F = 1meV$ we get $n \approx 10^8/cm^2$.

The origin of this doping is not yet well understood. However, the most likely causes are trapped charges and absorbed species at edges/defects etc. Recent STM experiments using graphene films doped on purpose with nitrogen (N) were aimed at characterizing at atomic scales the electronic structure modifications due to individual dopants [44]. It was found that N, which bonds with the carbon in the lattice, can contribute to the total number of mobile carriers in graphene resulting in a shift of the Dirac point. Moreover, the electronic properties of graphene are modified around an individual N dopant on length scales of only a few atomic spacings [44].

The existence of electron-hole puddles was first pointed out by single electron transistor studies with a spatial resolution of a hundred nm [6]. Higher resolution studies of the spatial fluctuations of the carrier distribution using STM showed even finer density fluctuations on nm scales [7]. The typical variation in the Dirac point of graphene deposited on SiO_2 was found to be 30-50meV corresponding to carrier densities of $(2 \times 10^{11} - 4 \times 10^{11})cm^{-2}$ [6, 7, 9].

In the presence of scattering centers, the electronic wave functions can interfere to form standing wave patterns which can be observed by measuring the spatial dependence of dI/dV at a fixed sample bias voltage. By using these interference patterns, it was possible to discern individual scattering centers in the dI_t/dV_{Bias} maps obtained at energies far from the Dirac point when the electron wave length is small. No correlations were found between the corrugations and the scattering centers, suggesting that the latter play a more important role in the scattering process. When the sample bias voltage is close to the Dirac point, the electron wave length is so large that it covers many scattering centers. Thus, the dI_t/dV_{Bias} maps show coarse structures arising from the electron-hole puddles. The Fourier transform of the interference pattern provides information about the energy and momentum distribution of quasiparticle scattering, which can be used to infer band structure information [45]. For unperturbed single layer graphene, interference patterns are expected to be absent or very weak [46]. However, due to the strong scattering centers, clear interference patterns are observed for graphene on SiO_2 [7], where the main scattering centers are believed to be trapped charges.

In contrast to graphene on SiO_2, graphene on graphite shows very little variation of the Dirac point ($\approx$ 5meV) across hundreds of nm [14, 34] (Figure 5(b)). This is illustrated in the spatial map of the distance between the Dirac point and the Fermi level shown in Figure 5(a). The value of the Dirac point was extracted by fitting the Landau level sequence, as discussed in the next section. Further demonstration of the homogeneity of the graphene flakes on graphite is given by the Fermi velocity which is found to vary by less than 5% across the same area as shown in Figure 5(c),(d). For the histogram is Figure 5(d) the mean value of the velocity is $v_F = 0.78 \times 10^6 ms^{-1}$. Similarly, the fluctuations of the local charge density in graphene on h-BN were recently found to be much smaller than on SiO_2 [32, 33].

2.4   Landau levels

In the presence of a magnetic field, B, normal to the plane, the energy spectrum of 2D electron systems breaks up into a sequence of discrete Landau levels (LL). For the non-relativistic case realized for example in the 2D electron system on helium [47] or in semiconductor heterostructures [48], the Landau level sequence consists of a series of equally spaced levels similar to that of a harmonic oscillator: $E = \hbar\omega_c(N+1/2)$ with the cyclotron frequency $\omega_c = eB/m^*$,
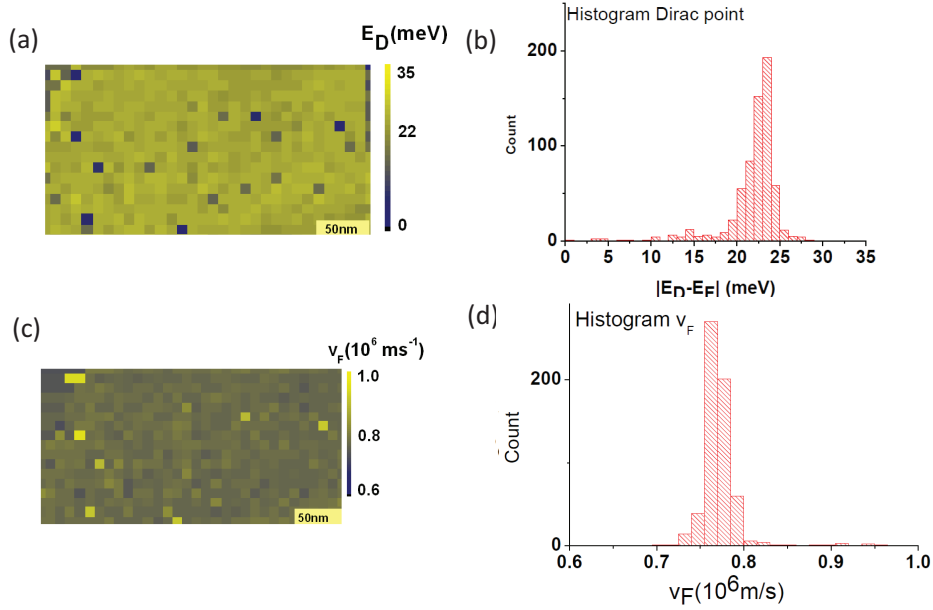
Figure 5: (a) Map of the Dirac point on graphene on graphite [14]. (b) Histogram of the values of Dirac point in (a). (c) Map of the Fermi velocity on graphene on a graphite substrate [14]. (d) Histogram of the velocities in (c).

a finite energy offset of $1/2\hbar\omega_c$, and an effective mass m^*. In graphene, as a result of the linear dispersion and Berry phase of π, the Landau level spectrum is different:

$$E_n = \pm\hbar\omega_G\sqrt{|N|}, \omega_G = \frac{\sqrt{2}v_F}{l_B} \tag{7}$$

Here, $N = ... -2, -1, 0, +1, +2...$ is the index of the Landau level, ω_G is the cyclotron energy for graphene and $l_B = \sqrt{\frac{\hbar}{eB}}$ is the magnetic length.

Compared to the non-relativistic case the energy levels are no longer equally spaced, the field dependence is no longer linear and the sequence contains a level exactly at zero energy, $N = 0$, which is a direct manifestation of the Berry phase in graphene [49]. We note that the LLs are highly degenerate, the degeneracy per unit area being equal to $4B/\phi_0$. Here B/ϕ_0 is the orbital degeneracy with $\phi_0 = h/e$ the flux quantum and $4 = g_s \cdot g_v$, where g_s and g_v ($g_s=g_v=2$) are the spin and valley degeneracy, respectively.

In Figure 6 an illustration of the quantized LL is presented. The conical dispersion of graphene in the absence of a magnetic field is transformed into a sequence of Landau levels corresponding to electron carriers above the Dirac point (DP) and holes below it. In the density of states, represented on the left side, a LL corresponds to a peak in the DOS. The indexes of the LLs are indicated as $N < 0$ for holes and $N > 0$ for electrons. Assuming that the Fermi level is exactly at the DP (the case of neutral graphene), the gray area in Figure 6 represents electronic states that are already filled.

Experimentally, a direct way to study the quantized Landau levels is through STS as was demonstrated in early studies on HOPG [50, 51] and adsorbate-induced two dimensional electron gases (2DEGs) formed by depositing Cs atoms on an n-InSb(110)surface [52].
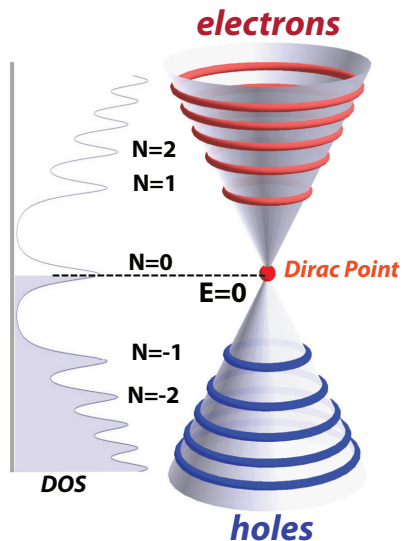
Figure 6: Illustration of quantized energy levels in graphene and their signature in the density of states. Right side: Dirac cone which in a magnetic field no longer has a continuum energy, but discrete levels: red rings for electrons, blue rings for holes. Left side: the vertical axis is energy; the horizontal axis is the density of states. For each Landau level there is a peak in the density of states which is broadened by electron-electron interactions in ideal systems. In the presence of disorder, the LL are further broadened. The indexes of the LLs are N=0 for the one at the Dirac point and N=+1,+2,+3... for the electron side and N=-1,-2,-3,... for the hole side.

2.4.1 Landau Levels in almost ideal graphene

STM studies of graphene flakes on graphite in a magnetic field by Li et al. [34] gave direct access to the LL sequence and its evolution with magnetic field. The main results are presented in Figure 7. In Figure 7(a) the high resolution spectrum at 4T shows sharp LL peaks in the tunneling conductivity dI_t/dV_{Bias}. The field dependence of the STS spectra, shown in Figure 7(b), exhibits an unevenly spaced sequence of peaks flanking symmetrically, in the electron and hole sectors, a peak at the Dirac point. All peaks, except the one at the Dirac point, which is identified as N=0, fan out to higher energies with increasing field. The peak heights increase with field, consistent with the increasing degeneracy of the LL. To verify that this sequence of peaks does indeed correspond to massless Dirac fermions, the field and level-index dependence of the peak energies in the sequence was measured. It was then compared to the expected values (Equation (7)) measured relative to the Fermi energy (the convention in STS) as shown in Figure 7(c). This scaling procedure collapses all the data onto a straight line. Comparing to Equation (7), the slope of the line gives a direct measure of the Fermi velocity, $v_F = 0.79 \cdot 10^6 m/s$. This value is 20% less than expected from single particle calculations and, as discussed later, the reduction can be attributed to electron-phonon interactions. The presence of a N=0 field-independent state at the Dirac point together with the square-root dependence of the LL sequence on both field and level index, are the hallmarks of massless Dirac fermions.

The technique described above, Landau level spectroscopy, can be used to obtain the Fermi velocity of Dirac fermions, the quasiparticle lifetime, the electron phonon coupling, and the degree of coupling to the substrate [14, 53]. LL spectroscopy gives access to the

electronic properties of Dirac fermions when they define the surface electronic properties. This technique was adopted and successfully implemented to probe massless Dirac fermions in other systems including graphene on SiO_2 [9], epitaxial graphene on SiC [54], graphene on Pt [55] and topological insulators [56, 57].

An alternative, though less direct, method of accessing the LLs is to probe the allowed optical transitions between the LLs by using cyclotron resonance measurements. This was done on exfoliated graphene on SiO_2 [58, 59], epitaxial graphene [60] and graphite [15]. Other indirect methods include scanning electron transistor or similar capacitive techniques [61, 62].
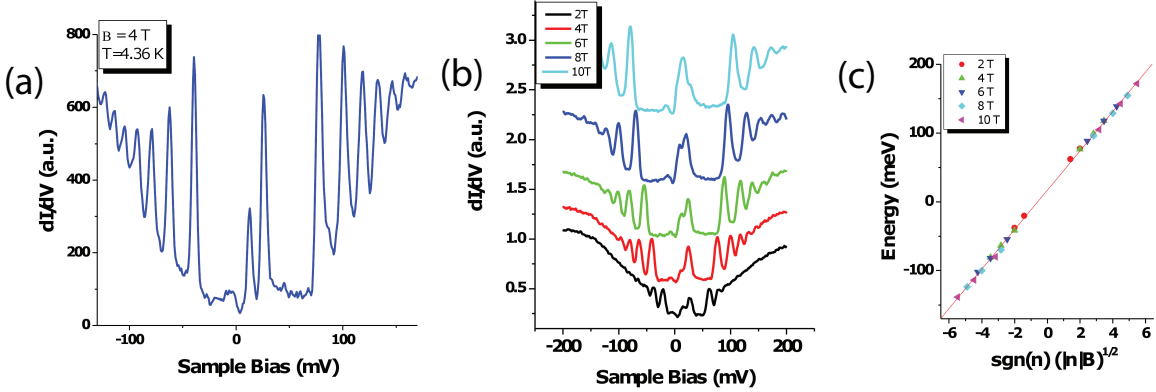
Figure 7: (a) STS spectrum of graphene on graphite showing the presence of Landau levels. (b) The evolution of the LLs with magnetic field. (c) The energy dependence of the LLs on the reduced parameter $sgn(N)\sqrt{|N|\,B}$ [34], where sgn refers to $\pm$ signs.

Electron-phonon interaction and velocity renormalization. The basic physics of graphene is captured in a tight-binding model. However, many-body effects are often not negligible. *Ab initio* density functional calculations show that the electron-phonon (e-ph) interactions introduce additional features in the electron self-energy, leading to a renormalized velocity at the Fermi energy [63]. Away from the Fermi energy, two dips are predicted in the velocity renormalization factor, $(v_F - v_{F0})/v_F$, at energies $E \pm \hbar\omega_{ph}$ where ω_{ph} is the characteristic phonon energy. At the energies of the phonons involved, such dips give rise to shoulders in the zero field density of states which can be measured in STS experiments.

Figure 8(a) plots the tunneling spectra measured on a decoupled graphene flake on graphite. Two shoulder features on both sides of the Fermi energy are seen around 150meV. These features are independent of tip-sample distance for tunneling junction resistances in the range $3.8-50G\Omega$. In Figure 8(b) the corresponding two dips in the renormalized velocity are visible. This suggests that the optical breathing phonon, A_1' with energy $E \approx 150meV$ plays an important role in the velocity renormalization observed in graphene [63]. The line width of the A_1' phonon decreases significantly for bilayer graphene and decreases even more for graphite [64, 65]. Therefore the electron-phonon coupling through the A_1' phonon is suppressed by interlayer coupling and the induced velocity renormalization is only observed in single layer graphene decoupled from the substrate.

Landau level linewidth and electron-electron interactions The lineshapes of the LLs for the case of graphene on graphite were found to be Lorentzian rather than Gaussian [34], suggesting that the linewidth reflects the intrinsic lifetime rather than disorder broadening. Furthermore, looking closer at the linewidth of the LLs in Figure 8(c), it is found that the width increases linearly with energy. This dependence is consistent with the theoretical pre-

11

dictions that graphene displays a marginal Fermi liquid behavior: $\tau \propto E^{-1} \approx 9ps$ [66].
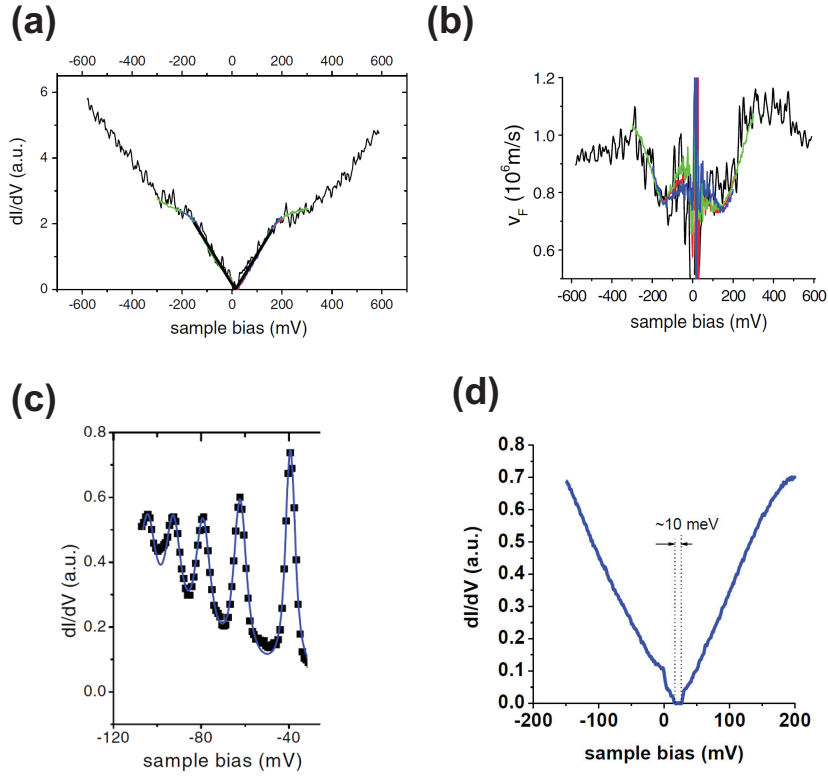
Figure 8: (a) STS data for graphene flakes on HOPG showing how the Fermi velocity is renormalized below a certain energy ($\approx$150meV). (b) The calculated renormalization of the Fermi velocity versus sample bias from the data in (a). (c) Fit of the LL lineshape with Lorentzians. (d) Tunneling spectra taken with higher resolution revealing a 10meV gap at the Dirac point [34].

Another interesting feature is the presence of an energy gap with $E_{gap} \approx 10meV$ in the B=0T spectrum as shown in 8(d) which may have the same origin as the splitting of the $N = 0$ level in finite field. One possible explanation for the presence of this gap is the broken A-B symmetry due to the Bernal stacking of the graphene layer with respect to the graphite substrate, but more work is needed to elucidate its origin.

Lifting of the LL degeneracy was observed in quantum Hall effect measurements on the highest quality suspended graphene devices [67, 68] and in STM experiments on epitaxial graphene on SiC [69].

2.4.2   Effects of interlayer coupling

For graphene flakes on graphite one can also address the effect of interlayer coupling in regions where the graphene flakes are weakly coupled to the substrate. It was found that the LL spectrum of graphene which is weakly coupled to a graphite substrate strongly depends on the degree of coupling.

In Figure 9(a) the topography image shows two regions: G, where the top layer is decoupled and displays signatures of a single layer graphene and below it, a different region, W, where there is weak coupling to the underlying graphite substrate. In the presence of weak coupling the LL spectrum changes into a complex sequence resulting from splittings of the levels due to

lifted level degeneracy. This is illustrated by the spatial dependence of the LLs in Figure 9(b) where the LL sequence changes after crossing the boundary between G and W [14]. By fitting the LL sequence in W to the theoretical model described in [53], the coupling was found to be a tenth of the one in a regular Bernal stacked bilayer [14].
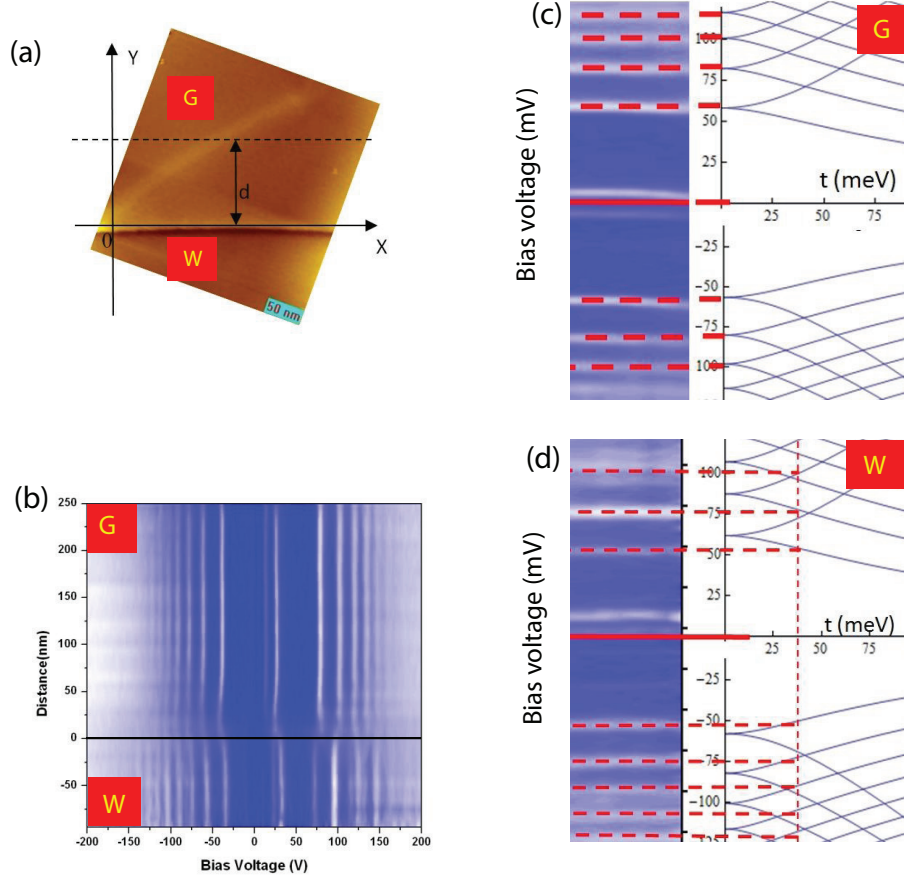
Figure 9: (a) STM image showing two distinct regions: G- where the graphene flake is decoupled from graphite; W- where the graphene flake is weakly coupled to the graphite substrate. (b) The evolution of the Landau levels from region G to region W. The vertical axis is the position where the spectrum is measured indicated by d in (a); the horizontal axis is the sample bias. (c),(d) Fits of the LLs in (b) to the theoretical model [53], in which t is the coupling parameter between the layers, for no coupling (c) and weak coupling (d) [14].

2.4.3   Landau Levels in disordered graphene

For graphene device applications which require gating and the ability to do transport measurements, it is necessary to use insulating substrates. Therefore, although the quality of graphene on graphite is far superior to that on an insulating substrates, graphite substrates cannot be used in practical applications.

Initially, the disorder potential found on standard SiO_2 substrates, was too large to allow observation of LLs by STS even in the highest magnetic fields [41] so further improvement of the substrate was needed. One procedure that was demonstrated to dramatically improve sample quality is to remove the SiO_2 substrate under the graphene which becomes suspended

[67, 68, 70, 71]. However, such samples are fragile and small, so studying them is challenging.

Therefore, exploring ways to improve the substrate is of interest. In the semiconductor industry it is known that the quality of SiO_2 can be greatly improved using dry oxidation in the presence of chlorine. This process reduces the number of trapped charges in the oxide, improving the uniformity and quality of the insulator [72, 73, 74, 75]. When using such substrates treated by chlorination, the STM and STS measurements show that it is possible to see well defined quantized levels for high enough magnetic fields [9]. The broadening of the LLs, however, together with the deviation from a V-shaped zero-field density of states, indicate that such samples are not ideal.

STS in zero field was used to give an estimate of the average length scale of the disorder, the electron-hole puddle size, $d \approx 20nm$ [9]. In order to observe well defined levels, the magnetic length should be at most $(d/2) \approx 10nm$, corresponding to a magnetic field $B = 6T$. In Figure 10(a) the STS data taken for graphene on chlorinated SiO_2 shows how indeed, for smaller fields, below 6T, the levels are not well defined, while above 6T in Figures 10(a),(b) they become clearly defined.

In such samples it is expected that the levels are broadened by disorder [76, 77, 78]. The measured width of the levels is typically $\gamma \approx 20 - 30meV$, much larger than on HOPG and corresponds to a carrier lifetime of $\tau \approx 22 - 32fs$ consistent with values obtained by different techniques [58, 61, 62].

The Fermi velocity obtained by LL spectroscopy is $v_F = (1.07 \pm 0.02) \cdot 10^6 m/s$ (Figure 10(d)) and varies by $5 - 10\%$ depending on the position on the sample. To further illustrate the effect of disorder on the LLs, Figure 10(c) shows how the sequence of levels changes along a 60nm long line across the sample. The variation in brightness indicates spatial dependence of the LLs width and height due to disorder.

2.4.4 Gate dependence of Landau levels

Due to its band structure, in particular the electron-hole symmetry, graphene shows an ambipolar electric field effect. STS of gateable graphene on an insulating substrate can be used to study the evolution of the electronic wave function and density of states as the Fermi energy is moved through the LLs. The ability of STS to access both electron and hole states makes this a particularly powerful technique. In an STS experiment E_F is usually situated at zero bias and therefore it is convenient to define the E_F as the origin of the energy axis and to measure the Dirac point energy with respect to it.

Figure 11(a) shows a set of data taken at B=12T in which the spectrum was recorded for different gate voltages. Each vertical line is a spectrum at a particular gate voltage V_G. The intensity of the plot represents the value of the dI/dV, the lighter color corresponding to the peaks in the spectrum. The vertical axis is the sample bias and the horizontal axis is the gate voltage. The gate voltage was varied in the range $-15V < V_G < +43V$ corresponding to carrier densities: $3 \times 10^{12} cm^{-2} > n_c > -0.5 \times 10^{12} cm^{-2}$. In the spectrum taken at V_G=-15V a very faint N=0 level is seen at $\approx 240meV$. Because the sample was hole doped at neutral gate voltage already, in the energy range that we probe, we only measure the Landau levels corresponding to hole states: $N = -1, -2, -3....$ At higher gate voltages though, for $V_G > 40V$ the levels corresponding to electron states $N = +1, +2, +3...$ also become visible.

Qualitatively, one can understand the overall step-like features in Figure 11 (plateaus followed by abrupt changes in slope) as follows: the LL spectrum contains peaks, corresponding to high DOS, separated by regions of low DOS (Figure 11(a)). It takes a large change in the charge carrier density to fill the higher DOS regions - therefore plateaus appear; at this point the Fermi level is pinned to the particular Landau level being filled. On the other hand, filling the regions of low DOS in between the LLs does not require much change in carrier density
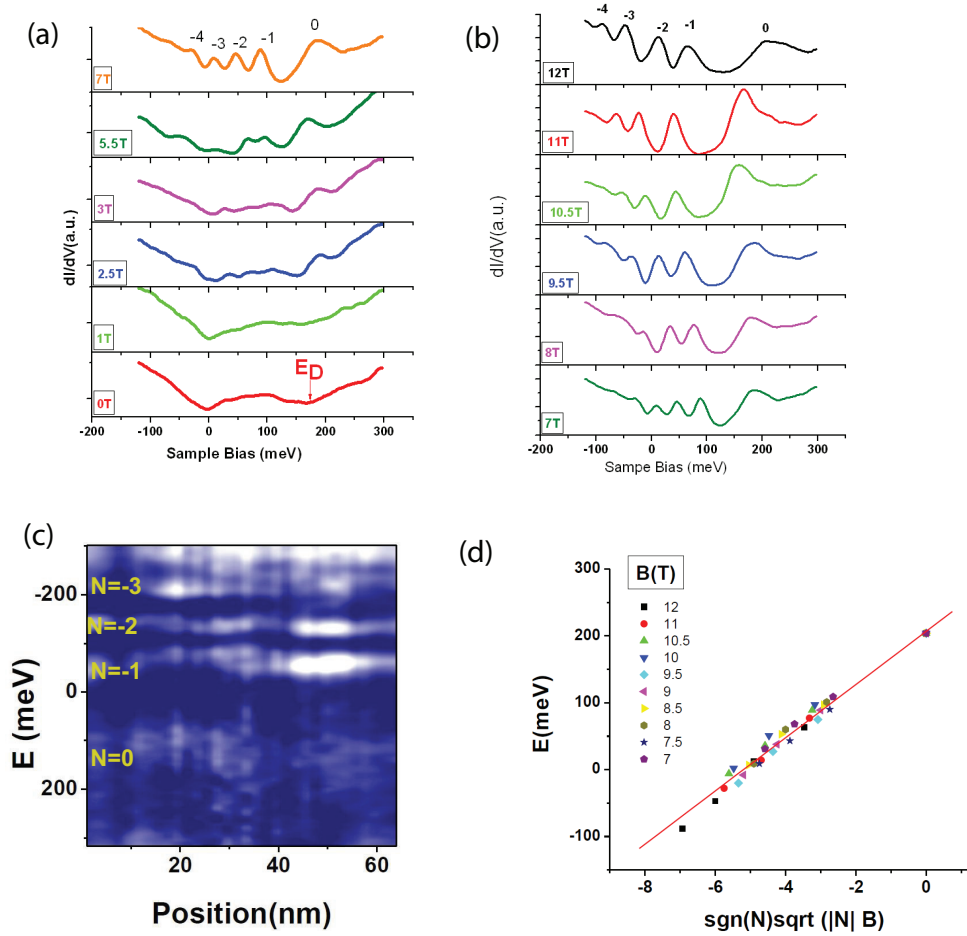
Figure 10: (a) STS data for graphene on SiO_2 for magnetic fields up to 7T. (b)STS data on graphene on SiO_2 for magnetic fields between 7T and 12T. (c) Example of typical evolution of the LL across a line of 60nm for the graphene on SiO_2 sample in B=10T. (d) Fermi velocity extracted from the LL sequence in (a) and (b) [9]. The energies of the LLs were shifted so that the Dirac point is the same for all fields. The spread in the LLs for different fields reflects slight variations of the Fermi velocity due to the fact that the spectra for the different fields were not taken at the exact same location on the sample.

- therefore an abrupt change in slope appears. For broad Landau levels the DOS in between the peaks is larger, thus smearing the step-like pattern.

A simulation considering the LL broadening and using v_F =(1.16 ± 0.02)x10^6 m/s is plotted in Figure 11(b) and shows good agreement with the measured data in Figure 11(a).

Similar experiments on graphene exfoliated on SiO_2, probing areas of different disorder across the sample, where reported by Jung et al. [36].

In the two-dimensional electron system (2DES) of very high mobility GaAs samples, this pinning of the Fermi level to the LL was observed by time domain capacitance spectroscopy [79].

In contrast to electrical transport measurements that typically probe states near the Fermi surface, STS can access both filled and empty states. Therefore, in a magnetic field, through LL spectroscopy one can probe the full shape of the Dirac cone in the measured energy range.

The shape of the cone was investigated as a function of carrier concentration by measuring the Fermi velocity from the LL sequence as a function of doping. Within the investigated range of charge carrier density ($3 \times 10^{12} cm^{-2} > n_c > -0.5 \times 10^{12} cm^{-2}$), it was found that closer to the Dirac point, the velocity increases by $\approx 25\%$ as seen in Figure 11(c).

At low carrier density the effects of electron-electron interactions and reduced screening on the quasiparticle spectrum are expected to become important. The observed increase in the Fermi velocity is consistent with a renormalization of the Dirac cone close to the neutrality point due to electron-electron interactions [66, 80]. If the random potential is further reduced such that LLs can be observed already in small fields, the fact that the spacing between the levels is smaller will make it possible to probe the reshaping of the cone with higher accuracy.

A similar result was obtained by Elias et al. on suspended graphene samples by measuring the amplitude of the Shubnikov de Haas oscillations as a function of temperature [81].
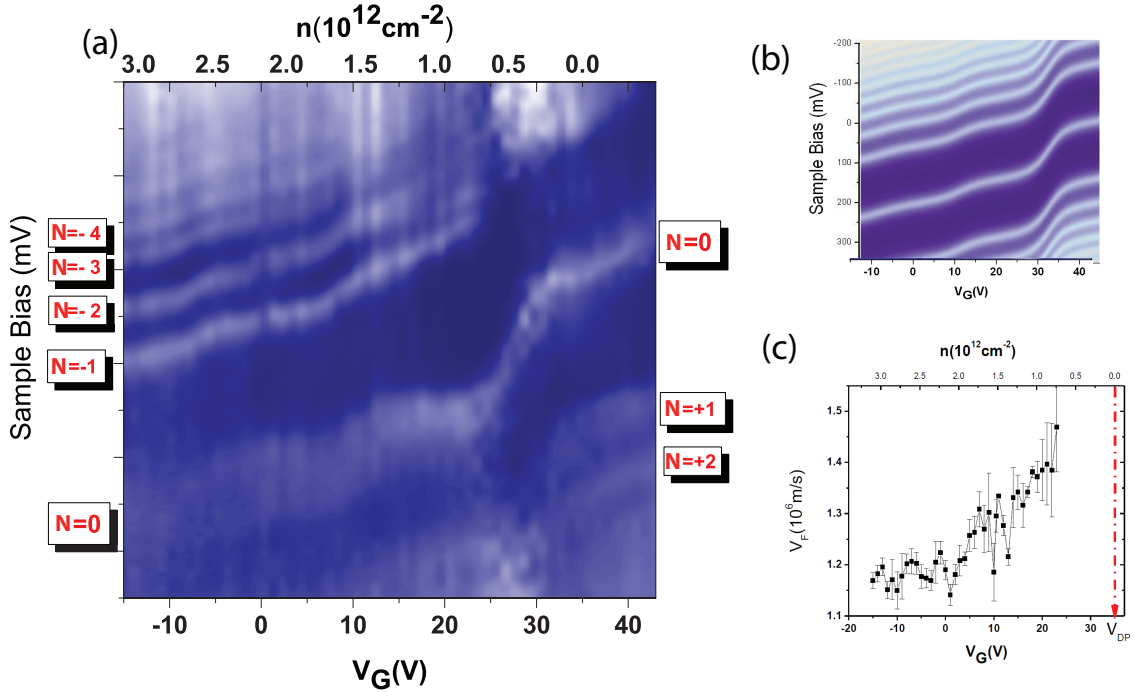
Figure 11: (a) Map of the dependence of the LL in graphene on SiO_2 on charge carrier density for B=12T. The vertical axis is the sample bias, the bottom horizontal axis is the gate voltage and the upper horizontal axis is the corresponding charge carrier density. The LL indexes are marked N=...$\pm 3, \pm 2, \pm 1, 0$. (b) Simulation of the evolution of the LL spectrum in (a). (c) Gate voltage dependence of the Fermi velocity. The Dirac point, at $V_G = 35$ V, is marked.

2.4.5 Disorder effects: extended and localized states

Impurities and the resulting random potential strongly affect the electronic wave function in graphene. By measuring STS in the presence of a perpendicular magnetic field, one can visualize the wavefunctions corresponding to the LLs in real space.

To this end, STS spectra are acquired on a fine grid of points across a chosen area. At a particular energy one can plot an intensity map having the x,y spatial coordinates and as z-coordinate the value of the dI/dV ($\propto$ DOS) at that energy. This map will illustrate the density of states variation in real space.
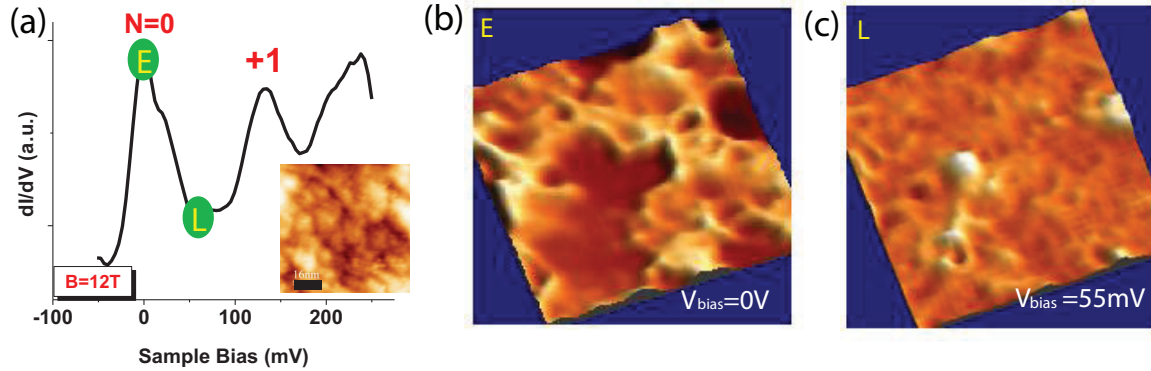
Figure 12: (a) Averaged tunneling spectra across the area in the inset showing LLs with index N=0,+1,... . The letters E and L indicate the energies where the STS maps in (b) and (c) are taken. The scale bar of the inset is 16nm. (b) STS map across the area in the inset of (a) at $V_{bias} = 0V$. (c) STS map across the area in the inset of (a) at $V_{bias} = 55mV$ [82].

Such a procedure is shown in Figure 12. Figure 12(a) represents the average over spectra taken in B=12T over a grid of points across the area of the sample shown by the STM image in the inset. The LLs with indexes N=0,+1,+2... are resolved at this field value. Figure 12(b) and (c) are the dI_t/dV_{bias} maps at energies marked in (a) as E and L where I_t is the tunneling current and V_{bias} is the bias voltage. At E $\approx$ 0 eV corresponding to the peak of the N=0 LL, Figure 12(b) shows bright regions of high DOS forming an extended percolating state. At E $\approx$ 55 meV in between N=0 and N=+1, Figure 12(c) shows the complementary localized states around impurities [82].

The presence of extended and localized states on the peaks and valleys of the LL spectrum is often used to qualitatively understand the integer quantum Hall effect (IQHE). A typical IQHE measurement in a Hall bar configuration [83] measures the Hall (transverse) resistivity ρ_{xy} and the longitudinal resistivity ρ_{xx} while varying the filling factor $\nu = (n_s h)/(eB)$ with n_s the carrier density, B the magnetic field, h the Planck constant and e the electron charge.

When the filling is such that the Fermi level lies in between two LLs the electrons are trapped in the localized states around the impurities and they do not play any role in the conduction. At this point $\rho_{xx} = 0$ and ρ_{xy} is quantized. When the Fermi level is at a peak of a Landau level, the electrons occupy the percolating state across the sample so ρ_{xx} is finite and ρ_{xy} increases making the transition between the quantized plateaus.

STM/STS experiments probing the extended and localized quantum Hall states were reported on the adsorbate-induced two dimensional electron gas on n-InSb(110) [52] and on epitaxial graphene on SiC [84].

2.5 Measuring small graphene devices with scanning probes

The discovery of graphene opened exciting opportunities to study a 2D system by surface probes. However the fact that the cleanest samples obtained by exfoliation are only a few microns in size poses technical challenges. Some room temperature experimental set-ups containing optical microscopes can overcome this problem. Even low temperature experiments which are equipped with long range optical microscopes or scanning electron microscopes can find small samples, but most low temperature and magnetic field setups are lacking such tools. For this reason, a capacitive method was developed in order to guide the STM tip towards micron size samples as detailed in [85].
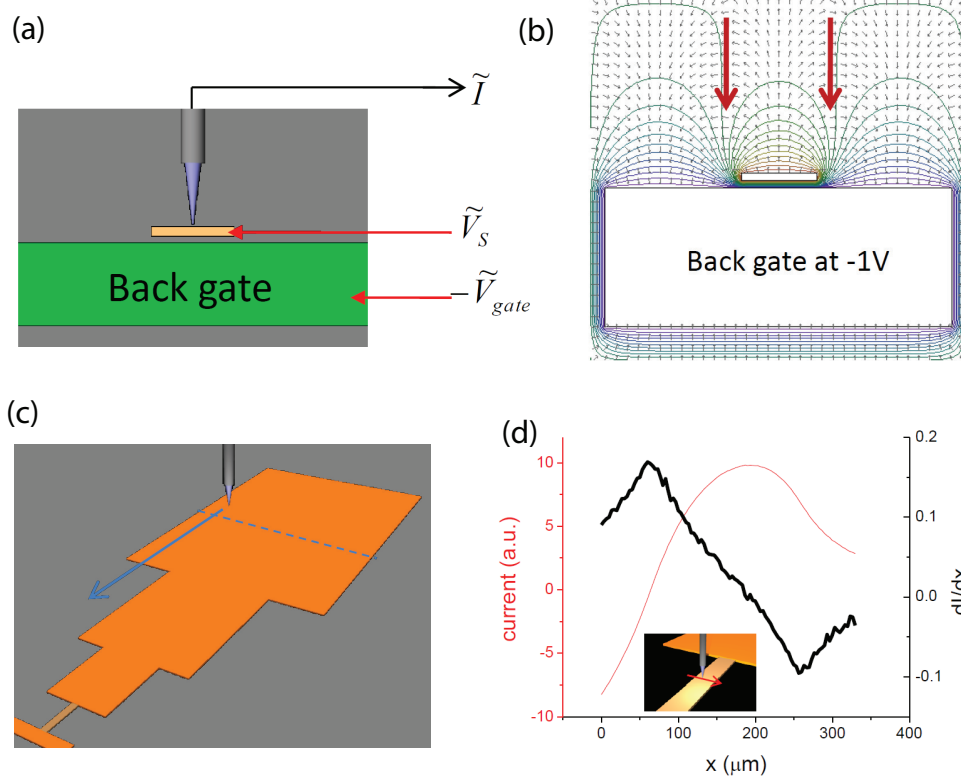
Figure 13: (a)General set-up of the sample separated by a SiO_2 layer from the back gate and the quantities of interest: pick-up current $\tilde{I}$, the ac voltage applied to the sample $\tilde{V}_s$, and the gate voltage $\tilde{V}_{gate}$. (b) Electric field lines above the sample when the tip is not taken into account, but only the sample at V=+1V and the back gate at V=-1V. The arrows point to the edges of the sample. (c) Sketch of the metallic lead connected to the sample. The tip will travel across the largest pad on the indicated dashed line and after that towards the smaller pad as pointed by the arrow. (d) The typical measured current versus position for the tip moving across one of the pads as well as its derivative.

To measure STS one usually applies a small ac modulation to the sample bias voltage, $\tilde{V}_s$, so that there is an ac current, $\tilde{I}$, flowing through the STM tip: $\tilde{I} = G_t \cdot \tilde{V}_s + i\omega C \tilde{V}_s$, where G_t is the tunneling conductance and C is the tip-sample capacitance. The contributions to the ac current are from tunneling (first term) and from capacitive pickup (second term). The pick-up signal can be used to resolve small structures when the tip is far from the surface and it is not in the tunneling regime.

The schematic set up for this method is shown in Figure 13 (a). The output voltage from the reference channel of a lock-in amplifier is split into two with 180° phase shift between them. One of the signals (+) is applied to the sample directly as $\tilde{V}_s$, the other (-) is applied to the gate $-\tilde{V}_{gate}$ through a pot resistor to adjust the amplitude. The capacitive pickup current measured from the tip is $\tilde{I}$. One key aspect of the procedure is tuning the voltage applied to the back gate in order to minimize the background pick-up current as detailed in [85].

To qualitatively illustrate the sensitivity of this method in detecting sample edges, Figure 13 (b) shows the electric field lines around the sample, when $V_s = 1V$ and $V_{gate} = -1V$, highlighting the presence of steep potential lines at the edges of the sample.

Another novel component is the design of the metallic lead connected to the sample. This lead is made of connected pads which are becoming smaller in size closer to the sample, as

shown in a sketch of the typical design in Figure 13(c). This contact pad geometry makes it possible to locate small (micron size) samples on large (mm size) substrates with an STM tip alone, without the aid of complicated optical microscopy setups.

The measured pick-up current across one of the pads is shown in 13(d). The vertical left axis is the measured current and the horizontal axis is the position on the pad. The signal is higher when the tip is above the pad and smaller when it is off the pad, riding on top of an overall background signal. In the derivative of this current with respect to position, the edges of the pad can be identified as seen in the Figure 13(d)-right vertical axis.

Such a signal is dependent on the tip-pad distance, so after the edges of a large pad have been identified, one can approach the tip to the conductive surface in the STM mode and retract a smaller number of steps in order to resolve the edges of the next smaller pad. The fact that the tip is far from the surface while moving across the large pads prevents it from crashing.

This procedure is repeated until the smallest pad and the sample are found. The sensitivity of this method is sufficient for finding samples of a few microns in size as demonstrated by Luican et al. [9].

2.6   Graphene edges

The two high symmetry crystallographic directions in graphene, zig-zag and armchair are described in Figure 14(a). A graphene flake can terminate in one of the two or it can have an edge that is irregular and contains a mixture of zig-zag and armchair. The type of edge is predicted to have a significant impact on its electronic properties [87, 88].

One of the highest resolution imaging experiments of a graphene edge was done using Transmission Electron Microscopy [89]. However, to simultaneously characterize the atomic structure and probe the electronic properties of the graphene edges, STM/STS are the techniques needed.

Theoretically, the zig-zag edge is predicted to have a localized state [90], i.e. a peak in the DOS at the Fermi level. Experimentally this was observed on HOPG by STM experiments [91]. To determine the structure of the edges with STM, one compares the direction of the edge with the one of the graphite lattice which can be measured inside the sample. Once the type of edge was inferred from topography, Niimi et al. [91] found that when the spectrum is measured on a zig-zag edge, it shows a peak close to the Fermi level which is absent in the armchair case as expected from the theoretical calculations.

STM/STS experiments of graphene nanoribbons created by unzipping carbon nanotubes are able in principle to detect the presence of edge states and correlate them to the ribbon chirality [92].

However, to make a connection between the atomic structure of edges in graphene and the magneto-transport experiments showing integer quantum Hall effect or evidence of many-body physics, it is important to study graphene edges in a magnetic field. This was possible on graphene flakes on graphite. The topographic image in Figure 14(b) indicates the zig-zag edge as well as the positions where the spectra in Figure 14(c) were taken. The inset is the honeycomb lattice measured on the decoupled flake. Figure 14(c) shows the spectra obtained, in a perpendicular magnetic field B=4T, at distances from 0.5 l_B (top curve) to bulk (bottom curve). One feature that is unique to the zig-zag edge is the fact that while the higher index LLs get smeared closer to the edge, the N=0 is robust. The decay of the LL intensity upon approaching the edge is in good agreement with the theoretical prediction [93, 94] as shown in the inset of Figure 14(d).
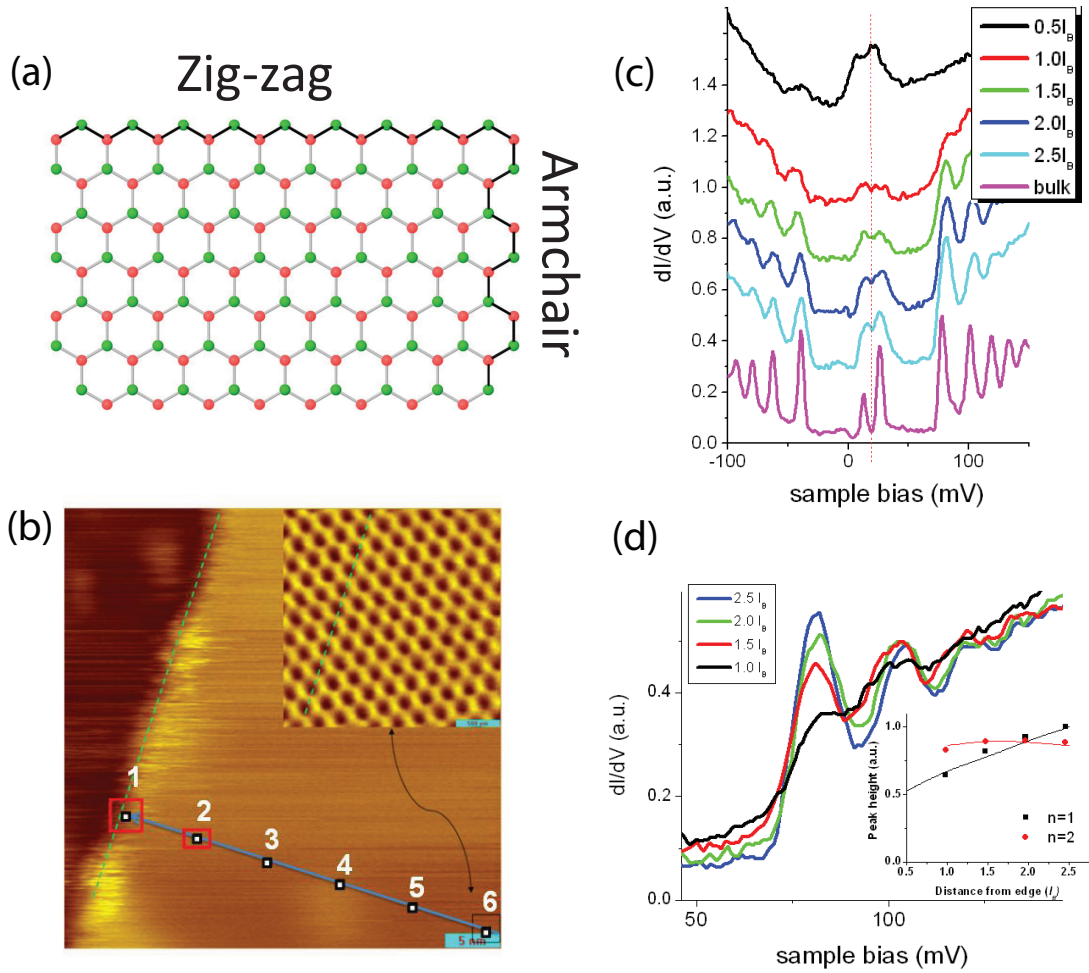
Figure 14: (a) Sketch of the two crystallographic directions: zig-zag and armchair edges. (b) Topography image of a decoupled graphene flake on graphite, its edge and the positions where the tunneling spectra were taken. The inset is the atomic resolution image obtained on the flake as indicated. (c) STS traces at various distances from the edge of the flake in (b) towards the bulk. (d) Evolution of the LL intensities moving towards the edge. Inset: Data points are heights of the peaks for N=1,2 and the curves are theoretical calculations [86].

2.7   Strain and electronic properties

Controlling strain in graphene is expected to provide new ways to tailor its electronic properties [95, 96]. Interestingly, as a result of strain in the lattice, the electrons in graphene can behave as if an external magnetic field is applied. The origin of this pseudo magnetic field is the fact that strain will introduce a gauge field in the Hamiltonian which mimics the presence of a magnetic field. In order to create a uniform field, however, the strain needs to be designed in particular configurations such as stretching graphene along three coplanar symmetric crystallographic directions [96].

Experimentally the effect of strain on the graphene spectrum was addressed by STM/STS measurements of graphene nanobubbles grown on a Platinum (111) surface [55]. On such samples, the peaks in the tunneling spectroscopy reported in [55] are interpreted as Landau levels originating from the pseudo magnetic field.

2.8 Bilayer graphene

Graphene layers stack to form graphite in the so-called Bernal stacking arrangement. If we name the two inequivalent atomic sites in the graphene lattice A and B, the top layer will have B atoms sitting directly on top of A atoms of the bottom layer and A atoms of the top layer sit above the centers of the hexagons of the graphene underneath. A system consisting of two layers of graphene in Bernal stacking, bilayer graphene, is characterized by a hyperbolic energy dispersion of its massive chiral fermions.

In the presence of a magnetic field the LL sequence for an ideal Bernal-stacked graphene sample is given by: $E_n = (\frac{e\hbar B}{m^*})\sqrt{N(N-1)}$ where m^* is the effective mass of the carriers, B is the magnetic field, e is the electron charge, $\hbar$ is Planck's constant divided by 2π and N=0,1,2,3,... . The eight fold degeneracy occurring for $N = 0, N = 1$ can be broken either by an applied electric field or by electron-electron interactions [97, 98, 99]. Experimentally, magneto-transport measurements of high quality suspended bilayer samples have revealed the presence of interaction-induced broken symmetry states [100, 101, 102].

In order to directly probe massive chiral fermions in bilayer graphene, STM/STS were performed on mechanically exfoliated graphene placed on insulating SiO_2 [103, 104]. It was found that the measured LL spectrum was dominated by effects of the disorder potential due to the substrate. The random potential creates an electric field between the two layers which results in locally breaking the LL degeneracy and a LL spectrum that is spatially nonuniform [104]. Therefore, in order to access the intrinsic properties of bilayer graphene, an improvement of samples that can be measured by STM/STS is necessary .

3 Electronic properties of twisted graphene layers

An infinitesimally small rotation away from Bernal stacking will completely change the electronic properties of the graphene bilayer system, suggesting the possibility of an extra knob to tune the electronic properties.

These rotational stacking faults are common and have been observed on graphite surfaces already in early STM studies [105, 106, 107, 108]. It was not until the discovery of graphene that the electronic properties have been investigated both theoretically and experimentally. With the new methods of preparing graphene by chemical vapor deposition it became even more important to address questions regarding the properties of rotated layers since the growth mechanism seems to favor the formation of twisted layers [21].

The consequence of superposing and rotating two identical periodic lattices with respect to each other is the formation of Moiré patterns. Considering two hexagonal lattices, the Moiré pattern emerging for an arbitrary rotation angle is illustrated in Figure 15(a). A commensurate pattern is obtained for discrete families of angles that can be mathematically derived [109, 110, 111, 112, 113, 114]. One such family of angles is: $cos(\theta_i) = (3i^2 + 3i + 1/2)/(3i^2 + 3i + 1)$ with $i = 0, 1, 2, ...$ The relation between the period of the superlattice L and the rotation angle θ is:

$$L = \frac{a}{2sin(\frac{\theta}{2})} \tag{8}$$

where $a \approx 0.246nm$ is the lattice constant of graphene.

STM can reveal areas where a Moiré pattern resulting from the twist of graphene layers is formed, as shown in Figure 15(b). In this case, the top graphene layer is misoriented with respect to the underlying graphite and has a Moiré pattern just until its boundary. Different angles will result in the formation of different patterns, as described by Eq. (8). Experimentally this is demonstrated by STM images showing superpatterns of different periodicity in
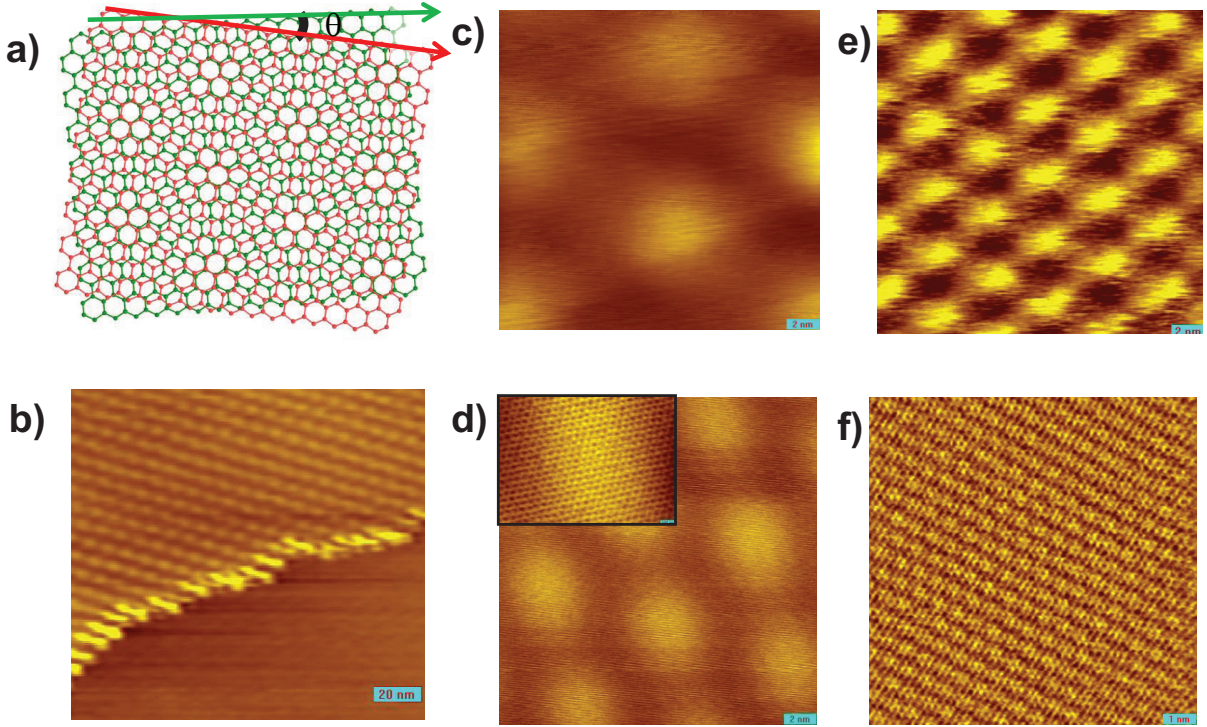
Figure 15: (a) Illustration of an emerging Moiré pattern from the rotation of two graphene layers. (b) STM topography image showing a Moiré pattern and its border in HOPG. (c)(d)(e)(f) STM images for Moiré patterns corresponding to angles 1.16 ^{o},1.79^o, 3.5^o, 21°, respectively [50, 115]. Scale bar in (c)-(e) 2nm, (f) 1nm

samples with different twist angles. For example, at rotation angle $\theta = 1.79^o$ the superperiod is $L = 7.7nm$. The sequence of four topographic maps in Figure 15(c),(d),(e),(f) have approximately the same field of view and they correspond to rotation angles of 1.16 ^{o}, 1.79^o, 3.5^o, 21°. The inset in Figure 15(d) (for $\theta= 1.79^o$) highlights the fact that the period of the atomic lattice of the graphene layer is much smaller than the Moiré pattern and can be visible on top of it. Typically the height observed in topography for the Moiré patterns is $\approx 0.1 - 0.3nm$.

3.1 Van-Hove singularities

In momentum space, the consequence of the twist between layers is the rotation of the corresponding Dirac cones with respect to each other as sketched in Figure 16(a). The distance between the cones is given by:

$$\Delta K = \frac{4\pi}{3a} 2sin(\frac{\theta}{2}) \tag{9}$$

At the intersections of the two Dirac cones their bands will hybridize, resulting in the key feature of the band structure, the two saddle points in both the electron and hole sides [109, 50]. The theoretical calculation of the dispersion in the case of rotation angle $\theta= 1.79^o$ is presented in Figure 16(b).

In two dimensions, the saddle points in the electronic band structure lead to diverging density of states, also known as Van Hove singularities (VHS)[116]. It is important to note

that in the absence of interlayer coupling, the Van Hove singularities will not appear. Corresponding to the saddle points in the dispersion shown in Figure 16(b), the VHS in the DOS are presented in Figure 16(c). The distance between the cones and implicitly between the saddle points is controlled by the rotation angle such that the distance in energy between the VHS depends monotonically on the angle θ. For the small angle regime, $2^o < \theta < 5^o$ the energy separation is: $\Delta E = \hbar v_F \Delta K - 2t^\theta$, where t^θ is the interlayer coupling. The rotation-induced VHSs are not restricted to the bilayer case. Qualitatively, if one layer is rotated with respect to a stack of layers underneath, the VHSs are still preserved.

To explore the angle dependence of VHSs, Li et al. [50] studied graphene layers prepared by chemical vapor deposition [21] as well as rotated graphene layers on graphite. The experimental data obtained from STS for different angles, $1.16^o, 1.79^o, 3.5^o$, is presented in Figure 16(d),(e),(f). The corresponding Moiré patterns are shown as insets. In each case, the measured spectra show two peaks, which are signatures of the VHS. The measured energy separation between the VHSs together with the theoretical curves are shown in Figure 16(g) indicating a monotonic increase with rotation angle.

An interesting situation arises in the limit of small angles [50]. Figure 17 (a) shows the measured topography of the Moiré pattern corresponding to $\theta = 1.16^o$. The spectrum in this case is presented in Figure 17(c) showing the two VHSs separated by a small energy $\Delta E \approx 12meV$. It is known that when the Fermi energy is close to the VHS, interactions, however weak, are magnified by the enhanced density of states, resulting in instabilities, which can give rise to new phases of matter [117, 118, 119]. This is consistent with the observation that the STS maps in Figure 17(b), taken at the energy of the singularity, suggest the formation of an ordered state such as charge a density wave. Such localization by Moiré patterns is also predicted by theoretical calculations [110].

3.2 Renormalization of the Fermi velocity

While for sufficiently separated cones, the low energy electronic bands still describe Dirac fermions, the slope of the Dirac cone is influenced by the Van Hove singularities, leading to a renormalized Fermi velocity.

Theoretically the equation describing the velocity renormalization was derived to be [109]

$$\frac{v_F(\theta)}{v_F^0} = 1 - 9\left(\frac{t_\perp^\theta}{\hbar v_F^0 \Delta K}\right)^2 \tag{10}$$

where v_F^0 is the bare velocity, $v_F(\theta)$ is the renormalized value at an angle θ; the interlayer coupling is $t_\perp^\theta \approx 0.4t_\perp$ and $t_\perp$ is the interlayer coupling in the Bernal stacked bilayer.

The curve corresponding to this relationship is plotted in Figure 18(g). For large angles $\theta > 15^o$ the renormalization effect is small, but the velocity is strongly suppressed for smaller angles.

In order to probe v_F, Luican et al. [115] measured the quantized LLs in a magnetic field and from their field and index dependence the velocity was extracted. For the large angle shown in Figure 18(a) the measured LL spectrum is presented in Figure 18(d). In this case of large angles, the low energy electronic properties are indistinguishable from those in a single layer and the measured $v_F = (1.10 \pm 0.01)10^6 m/s$.

In Figure 18(b)the topography image shows two adjacent regions B and C. In region B, a Moiré pattern with period of 4.0nm is resolved, while in region C, the pattern is not resolved, indicating an unrotated layer (or a much smaller period not resolved within the experimental resolution). In both regions STS in a magnetic field (Figure 18(e)) shows LL sequences specific
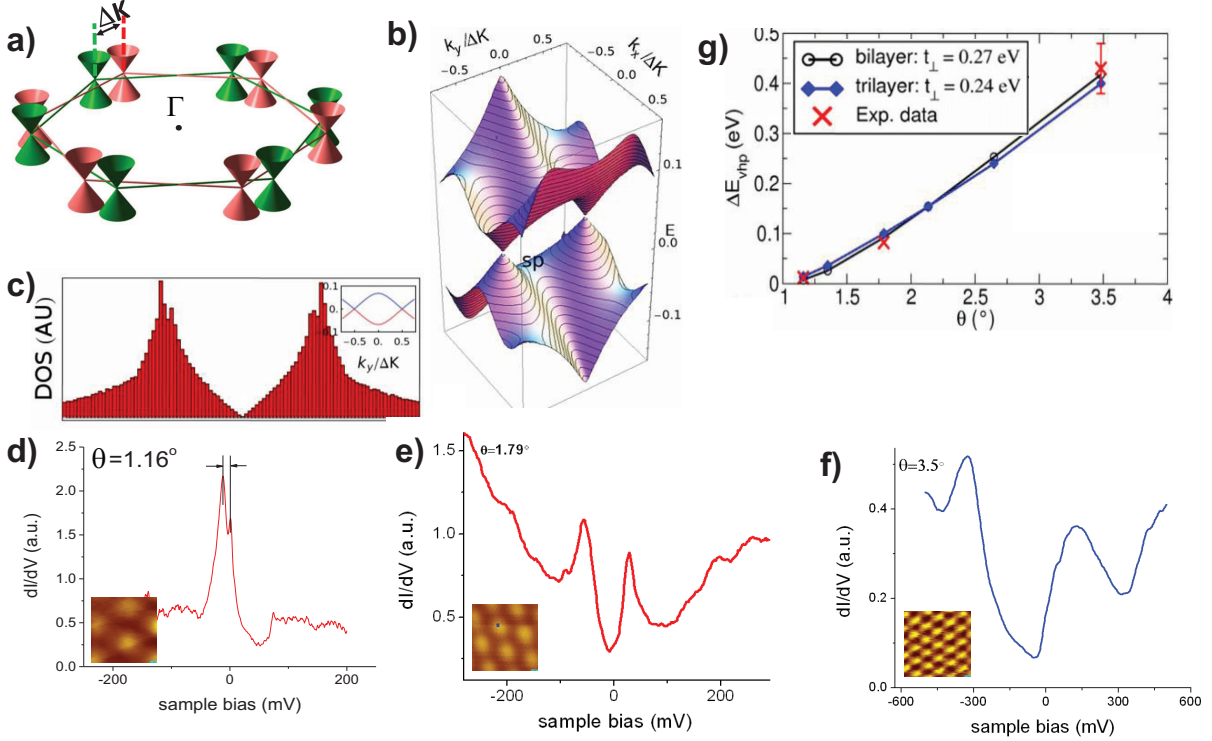
Figure 16: (a) The relative rotation in momentum space of the Dirac cones corresponding to two twisted graphene layers. (b) The calculated energy dispersion for two graphene layers rotated by $\theta = 1.79^o$. (c) The DOS corresponding to (b). The inset represents a cut through (b) along a line joining the two Dirac points. (d),(e),(f) STS for Moiré patterns corresponding to different angles, 1.16 ^{o},1.79^o, 3.5^o. The insets are the corresponding real space superpatterns. (g) Theoretical curves and experimental data obtained for the separation of VHSs as a function of rotation angle [50, 115].

to massless Dirac fermions with different Fermi velocities: 0.87x$10^6 m/s$ and 1.10x$10^6 m/s$ for regions B and C, respectively.

At very small angles, $\theta < 2^o$ such as the area in Figure 18(c), the VHSs become so dominant that massless Dirac fermions no longer describe the electronic states (Figure 18(f)). This regime is marked by a question mark in Figure 18(g).

It is important to note that the mechanism for renormalization of the Fermi velocity due to the presence of VHS is different from the case of graphene flakes on graphite discussed previously. In the twisted layers the renormalization is a sensitive function of the misorientation angle. In contrast, the velocity renormalization observed in the the case of graphene on graphite is due to electron-phonon interaction [34].

The results obtained on Moiré patterns on CVD graphene and graphite differ from the ones on epitaxially grown graphene on SiC [54, 120] which report a single layer graphene spectrum regardless of the twist angle. One clue towards understanding these results can be found in the unusual presence of a continuous atomic honeycomb structure across the entire Moiré superstructure in the case of epitaxial graphene. This is in contrast to Moiré patterns generated by two rotated layers where one sees a correlation between the Moiré pattern and the atomic structure which changes from triangular, to honeycomb, or in between the two, depending on the local stacking within the superpattern [108, 50].

If in addition to the twist of the top most layer, a Moiré pattern is present under the first
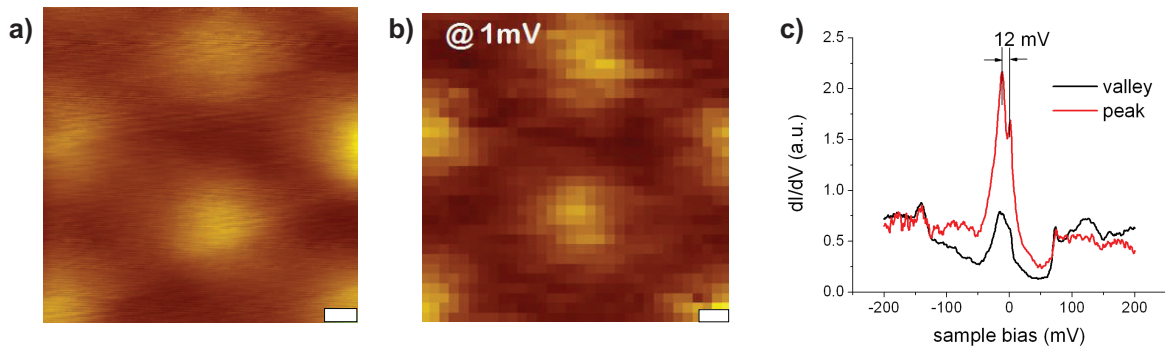
Figure 17: (a) Topography of a Moiré pattern corresponding to a small rotation angle : $\theta = 1.16^o$. The scale bar is 2nm. (b) dI_t/dV_{Bias} map taken at the area in (a) at energy E=1meV. The scale bar is 2nm. (c) STS on the peaks and valleys of the Moiré pattern in (a) [50].

layer (layer 2 rotated with respect to layer 3), it is expected that a complex superstructure involving several Moiré patterns will appear. This is the case in some of the experiments reported on epitaxially grown graphene on SiC [121]. In the case of the CVD graphene samples or graphite such multiple Moiré patterns were not observed. Therefore, the previously discussed features (VHS, reduction in Fermi velocity) are consequences of twisting only the top most layer with respect to the underlying single layer graphene or Bernal-stacked multilayer graphene.

4 Conclusions

In this chapter we presented a brief review of experimental results obtained by scanning tunneling microscopy and spectroscopy of graphene systems with various degree of disorder.

When the charge carriers are minimally affected by potential fluctuations in the substrate, as is the case for graphene flakes on the surface of graphite, one can access the intrinsic properties of the massless Dirac fermions in graphene. STS measurements show that the charge carriers in such flakes exhibit the hallmarks of massless Dirac fermions: the density of states is V-shaped and vanishes at the Dirac point and in the presence of a magnetic field the LL sequence contains a level at zero energy and follows the predicted square root dependence on field and level index. The quality of such samples allows access to physics beyond the the single particle picture and signatures of electron-phonon and electron-electron interactions can be studied.

Tuning the charge carrier concentration in graphene requires placing it on an insulating substrate such as SiO_2. In this case, graphene conforms to the rough surface of the oxide and the electrons are affected by the random potential introduced by the substrate. For this system, in the presence of a magnetic field, the Landau levels are broadened by disorder. The charge carrier density dependence of the LL spectrum shows pinning of the Fermi level at the respective LL which is filled. In such measurements that can probe the shape of the Dirac cone while tuning the carrier concentration, the velocity is found to increase upon reaching the Dirac point suggesting the onset of many body interactions.

Twisting graphene layers away from the equilibrium Bernal stacking leads to novel electronic properties. In the topographical images one can identify twisted graphene layers by the appearance of Moiré patterns dependent on the rotation angle. The twist gives rise to two Van
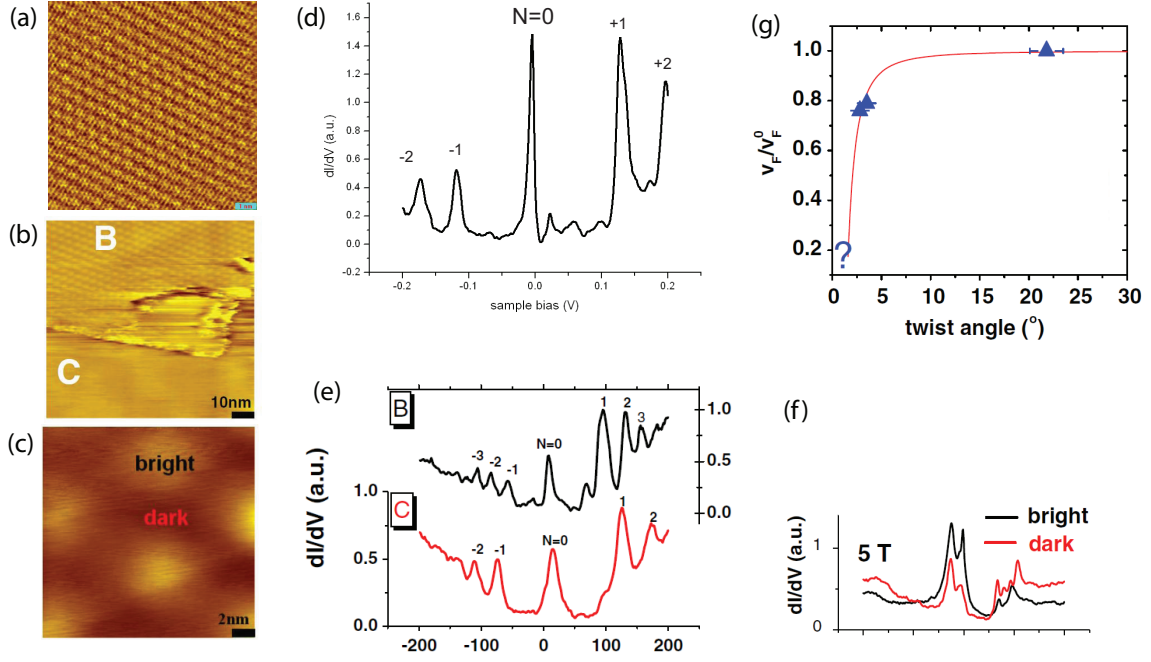
Figure 18: (a) STM of a Moiré pattern due to rotation $\theta = 21^o$. (b) STM of an area with two distinct regions: region B which has a Moiré pattern corresponding to rotation angle $\theta = 3.5^o$ and region C where there is no superpattern. (c) STM for a Moiré pattern with $\theta = 1.16^o$. (d) STS in a magnetic field showing the LL sequence measured in the area in (a). (e) STS in a magnetic field showing the spectrum for the area in (b) for regions B and C . (f) STS of the area in (c) for the dark and bright regions. (g) Plot of the theoretically predicted renormalization of the Fermi velocity together with the experimental values obtained from areas with different Moiré patterns [50, 115].

Hove singularities which flank the Dirac point symmetrically on the electron and hole sides and are centered at an energy that increases with the angle of rotation. The Fermi velocity of the charge carriers in the twisted layers is indistinguishable from single layer graphene for angles close to 30° , but v_F is dramatically reduced at very small angles.

Acknowledgments

References

[1] G. Binnig, H. Rohrer, Ch. Gerber, and E. Weibel. Surface studies by scanning tunneling microscopy. *Phys. Rev. Lett.*, 49(1):57–61, Jul 1982.

[2] J. Tersoff and D. R. Hamann. Theory of the scanning tunneling microscope. *Phys. Rev. B*, 31(2):805–813, Jan 1985.

[3] J. Bardeen. Tunnelling from a many-particle point of view. *Phys. Rev. Lett.*, 6(2):57–59, Jan 1961.

[4] G. Li, A Luican, and E.Y. Andrei. Electronic states on the surface of graphite. *Physica B: Condensed Matter*, 404(18):2673 – 2677, 2009.

[5] K.S. Novoselov, D. Jiang, F. Schedin, T.J. Booth, V.V. Khotkevich, S.V. Morozov, and A.K. Geim. Two-dimensional atomic crystals. *Proceedings of the National Academy of Sciences of the United States of America*, 102(30):10451, 2005.

[6] J. Martin, N. Akerman, G. Ulbricht, T. Lohmann, J.H. Smet, K. Von Klitzing, and A. Yacoby. Observation of electron–hole puddles in graphene using a scanning single-electron transistor. *Nature Physics*, 4(2):144–148, 2007.

[7] Y. Zhang, V.W. Brar, C. Girit, A. Zettl, and M.F. Crommie. Origin of spatial charge inhomogeneity in graphene. *Nature Physics*, 5(10):722–726, 2009.

[8] J.H. Chen, C. Jang, , S. Adam, M.S. Fuhrer, E.D. Williams, and M. Ishigami. Charged impurity scattering in graphene. *Nature Physics*, 4(5):377–381, 2008.

[9] A. Luican, G. Li, and E.Y. Andrei. Quantized Landau level spectrum and its density dependence in graphene. *Phys. Rev. B*, 83:041405, Jan 2011.

[10] C.R. Dean, A.F. Young, I. Meric, C. Lee, L. Wang, S. Sorgenfrei, K. Watanabe, T. Taniguchi, P. Kim, K.L. Shepard, and J. Hone. Boron nitride substrates for high-quality graphene electronics. *Nature Nanotechnology*, 5(10):722–726, 2010.

[11] C.R. Dean, A.F. Young, P. Cadden-Zimansky, L. Wang, H. Ren, K. Watanabe, T. Taniguchi, P. Kim, J. Hone, and K.L. Shepard. Multicomponent fractional quantum hall effect in graphene. *Nature Physics*, 7(9):693–696, 2011.

[12] C.H. Lui, L. Liu, K.F. Mak, G.W. Flynn, and T.F. Heinz. Ultraflat graphene. *Nature*, 462(7271):339–341, 2009.

[13] V. Geringer, M. Liebmann, T. Echtermeyer, S. Runte, M. Schmidt, R. Rückamp, M. C. Lemme, and M. Morgenstern. Intrinsic and extrinsic corrugation of monolayer graphene deposited on SiO_2. *Phys. Rev. Lett.*, 102(7):076102, Feb 2009.

[14] A. Luican, G. Li, and E.Y. Andrei. Scanning tunneling microscopy and spectroscopy of graphene layers on graphite. *Solid State Communications*, 149(27-28):1151–1156, 2009.

[15] P. Neugebauer, M. Orlita, C. Faugeras, A.L. Barra, and M. Potemski. How perfect can graphene be? *Physical Review Letters*, 103(13):136403, 2009.

[16] C. Berger, Z. Song, T. Li, X. Li, A.Y. Ogbazghi, R. Feng, Z. Dai, A.N. Marchenkov, E.H. Conrad, N. Phillip, et al. Ultrathin epitaxial graphite: 2d electron gas properties and a route toward graphene-based nanoelectronics. *The Journal of Physical Chemistry B*, 108(52):19912–19916, 2004.

[17] A.J. Van Bommel, J.E. Crombeen, and A. Van Tooren. LEED and Auger electron observations of the SiC(0001) surface. *Surface Science*, 48(2):463–472, 1975.

[18] I. Forbeaux, J.-M. Themlin, and J.-M. Debever. Heteroepitaxial graphite on $6h - $ SiC(0001) : interface formation through conduction-band electronic structure. *Phys. Rev. B*, 58:16396–16406, Dec 1998.

[19] K.S. Kim, Y. Zhao, H. Jang, S.Y. Lee, J.M. Kim, K.S. Kim, J.H. Ahn, P. Kim, J.Y. Choi, and B.H. Hong. Large-scale pattern growth of graphene films for stretchable transparent electrodes. *Nature*, 457(7230):706–710, 2009.

[20] Xuesong Li, Weiwei Cai, Jinho An, Seyoung Kim, Junghyo Nah, Dongxing Yang, Richard Piner, Aruna Velamakanni, Inhwa Jung, Emanuel Tutuc, Sanjay K. Banerjee, Luigi Colombo, and Rodney S. Ruoff. Large-area synthesis of high-quality and uniform graphene films on copper foils. *Science*, 324(5932):1312–1314, 2009.

[21] A. Reina, X. Jia, J. Ho, D. Nezich, H. Son, V. Bulovic, M.S. Dresselhaus, and J. Kong. Large area, few-layer graphene films on arbitrary substrates by chemical vapor deposition. *Nano letters*, 9(1):30–35, 2008.

[22] Q. Yu, L.A. Jauregui, W. Wu, R. Colby, J. Tian, Z. Su, H. Cao, Z. Liu, D. Pandey, D. Wei, et al. Control and characterization of individual grains and grain boundaries in graphene grown by chemical vapour deposition. *Nature Materials*, 10(6):443–449, 2011.

[23] S. Marchini, S. Günther, and J. Wintterlin. Scanning tunneling microscopy of graphene on Ru(0001). *Phys. Rev. B*, 76:075429, Aug 2007.

[24] P.W. Sutter, J.I. Flege, and E.A. Sutter. Epitaxial graphene on ruthenium. *Nature materials*, 7(5):406–411, 2008.

[25] Alpha T. N'Diaye, Sebastian Bleikamp, Peter J. Feibelman, and Thomas Michely. Two-dimensional Ir cluster lattice on a graphene Moiré on Ir(111). *Phys. Rev. Lett.*, 97:215501, Nov 2006.

[26] E. Loginova, S. Nie, K. Thürmer, N. C. Bartelt, and K.F. McCarty. Defects of graphene on Ir(111): Rotational domains and ridges. *Phys. Rev. B*, 80:085430, Aug 2009.

[27] P. Sutter, J. T. Sadowski, and E. Sutter. Graphene on Pt(111): Growth and substrate interaction. *Phys. Rev. B*, 80:245411, Dec 2009.

[28] A. Fasolino, J.H. Los, and M.I. Katsnelson. Intrinsic ripples in graphene. *Nature Materials*, 6(11):858–861, 2007.

[29] N.D. Mermin and H. Wagner. Absence of ferromagnetism or antiferromagnetism in one- or two-dimensional isotropic heisenberg models. *Physical Review Letters*, 17(22):1133–1136, 1966.

[30] M.I. Katsnelson and A.K. Geim. Electron scattering on microscopic corrugations in graphene. *Philosophical Transactions of the Royal Society A: Mathematical, Physical and Engineering Sciences*, 366(1863):195, 2008.

[31] J.C. Meyer, A.K. Geim, M.I. Katsnelson, K.S. Novoselov, T.J. Booth, and S. Roth. The structure of suspended graphene sheets. *Nature*, 446(7131):60–63, 2007.

[32] J. Xue, J. Sanchez-Yamagishi, D. Bulmash, P. Jacquod, A. Deshpande, K. Watanabe, T. Taniguchi, P. Jarillo-Herrero, and B.J. LeRoy. Scanning tunnelling microscopy and spectroscopy of ultra-flat graphene on hexagonal boron nitride. *Nature Materials*, 10(4):282–285, 2011.

[33] R. Decker, Y. Wang, V.W. Brar, W. Regan, H.Z. Tsai, Q. Wu, W. Gannett, A. Zettl, and M.F. Crommie. Local electronic properties of graphene on a bn substrate via scanning tunneling microscopy. *Nano Letters*, 11(6):2291–2295, 2011.

[34] G. Li, A. Luican, and E.Y. Andrei. Scanning tunneling spectroscopy of graphene on graphite. *Phys. Rev. Lett.*, 102(17):176804, Apr 2009.

[35] A. Deshpande, W. Bao, F. Miao, C.N. Lau, and B.J. LeRoy. Spatially resolved spectroscopy of monolayer graphene on SiO_2. *Physical Review B*, 79(20):205411, 2009.

[36] S. Jung, G.M. Rutter, N.N. Klimov, D.B. Newell, I. Calizo, A.R. Hight-Walker, N.B. Zhitenev, and J.A. Stroscio. Evolution of microscopic localization in graphene in a magnetic field from scattering resonances to quantum dots. *Nature Physics*, 7(3):245–251, 2011.

[37] E. Stolyarova, K.T. Rim, S. Ryu, J. Maultzsch, P. Kim, L.E. Brus, T.F. Heinz, M.S. Hybertsen, and G.W. Flynn. High-resolution scanning tunneling microscopy imaging of mesoscopic graphene sheets on an insulating surface. *Proceedings of the National Academy of Sciences*, 104(22):9209, 2007.

[38] M. Ishigami, J.H. Chen, W.G. Cullen, M.S. Fuhrer, and E.D. Williams. Atomic structure of graphene on SiO_2. *Nano Lett*, 7(6):1643–1648, 2007.

[39] A. H. Castro Neto, F. Guinea, N. M. R. Peres, K. S. Novoselov, and A. K. Geim. The electronic properties of graphene. *Rev. Mod. Phys.*, 81(1):109–162, Jan 2009.

[40] K. S. Novoselov, A. K. Geim, S. V. Morozov, D. Jiang, Y. Zhang, S. V. Dubonos, I. V. Grigorieva, and A. A. Firsov. Electric field effect in atomically thin carbon films. *Science*, 306(5696):666–669, 2004.

[41] V. Geringer, D. Subramaniam, A.K. Michel, B. Szafranek, D. Schall, A. Georgi, T. Mashoff, D. Neumaier, M. Liebmann, and M. Morgenstern. Electrical transport and low-temperature scanning tunneling microscopy of microsoldered graphene. *Applied Physics Letters*, 96:082114, 2010.

[42] Y. Zhang, V.W. Brar, F. Wang, C. Girit, Y. Yayon, M. Panlasigui, A. Zettl, and M.F. Crommie. Giant phonon-induced conductance in scanning tunnelling spectroscopy of gate-tunable graphene. *Nature Physics*, 4(8):627–630, 2008.

[43] M.L. Teague, A.P. Lai, J. Velasco, C.R. Hughes, A.D. Beyer, M.W. Bockrath, C.N. Lau, and N.C. Yeh. Evidence for strain-induced local conductance modulations in single-layer graphene on SiO_2. *Nano Letters*, 9(7):2542–2546, 2009.

[44] L. Zhao, R. He, K. T. Rim, T. Schiros, K. S. Kim, H. Zhou, C. Gutirrez, S. P. Chockalingam, C. J. Arguello, L. Palova, D. Nordlund, M. S. Hybertsen, D.R. Reichman, T.F. Heinz, P. Kim, A. Pinczuk, G. W. Flynn, and A.N. Pasupathy. Visualizing individual nitrogen dopants in monolayer graphene. *Science*, 333(6045):999–1003, 2011.

[45] G. M. Rutter, J. N. Crain, N. P. Guisinger, T. Li, P. N. First, and J. A. Stroscio. Scattering and interference in epitaxial graphene. *Science*, 317(5835):219–222, 2007.

[46] I. Brihuega, P. Mallet, C. Bena, S. Bose, C. Michaelis, L. Vitali, F. Varchon, L. Magaud, K. Kern, and J.Y. Veuillen. Quasiparticle chirality in epitaxial graphene probed at the nanometer scale. *Physical Review Letters*, 101(20):206802, 2008.

[47] E.Y. Andrei. *Two-dimensional electron systems on helium and other cryogenic substrates*, volume 19. Kluwer Academic Pub, 1997.

[48] John H. Davies. *The physics of low-dimensional semiconductors: an introduction*. Cambridge Univ Pr, 1998.

[49] G.W. Semenoff. Condensed-matter simulation of a three-dimensional anomaly. *Physical Review Letters*, 53(26):2449–2452, 1984.

[50] G. Li and E.Y. Andrei. Observation of Landau levels of Dirac fermions in graphite. *Nature Physics*, 3(9):623–627, 2007.

[51] T. Matsui, H. Kambara, Y. Niimi, K. Tagami, M. Tsukada, and Hiroshi Fukuyama. STS observations of Landau levels at graphite surfaces. *Phys. Rev. Lett.*, 94:226403, Jun 2005.

[52] K. Hashimoto, C. Sohrmann, J. Wiebe, T. Inaoka, F. Meier, Y. Hirayama, R. A. Römer, R. Wiesendanger, and M. Morgenstern. Quantum Hall transition in real space: from localized to extended states. *Phys. Rev. Lett.*, 101:256802, Dec 2008.

[53] J.M. Pereira Jr, F.M. Peeters, and P. Vasilopoulos. Landau levels and oscillator strength in a biased bilayer of graphene. *Physical Review B*, 76(11):115419, 2007.

[54] D.L. Miller, K.D. Kubista, G.M. Rutter, M. Ruan, W.A. De Heer, et al. Observing the quantization of zero mass carriers in graphene. *Science*, 324(5929):924, 2009.

[55] N. Levy, S. A. Burke, K. L. Meaker, M. Panlasigui, A. Zettl, F. Guinea, A. H. Castro Neto, and M. F. Crommie. Strain-induced pseudomagnetic fields greater than 300 tesla in graphene nanobubbles. *Science*, 329(5991):544–547, 2010.

[56] P. Cheng, C. Song, T. Zhang, Y. Zhang, Y. Wang, J.F. Jia, J. Wang, Y. Wang, B.F. Zhu, X. Chen, et al. Landau quantization of topological surface states in Bi_2Se_3. *Physical Review Letters*, 105(7):76801, 2010.

[57] T. Hanaguri, K. Igarashi, M. Kawamura, H. Takagi, and T. Sasagawa. Momentum-resolved Landau-level spectroscopy of Dirac surface state in Bi_2Se_3. *Phys. Rev. B*, 82:081305, Aug 2010.

[58] Z. Jiang, E.A. Henriksen, L.C. Tung, Y.J. Wang, M.E. Schwartz, M.Y. Han, P. Kim, and H.L. Stormer. Infrared spectroscopy of Landau levels of graphene. *Physical Review Letters*, 98(19):197403, 2007.

[59] R. S. Deacon, K.-C. Chuang, R. J. Nicholas, K. S. Novoselov, and A. K. Geim. Cyclotron resonance study of the electron and hole velocity in graphene monolayers. *Phys. Rev. B*, 76:081406, Aug 2007.

[60] ML Sadowski, G. Martinez, M. Potemski, C. Berger, and WA De Heer. Landau level spectroscopy of ultrathin graphite layers. *Physical Review Letters*, 97(26):266405, 2006.

[61] J. Martin, N. Akerman, G. Ulbricht, T. Lohmann, K. Von Klitzing, JH Smet, and A. Yacoby. The nature of localization in graphene under quantum Hall conditions. *Nature Physics*, 5(9):669–674, 2009.

[62] L. A. Ponomarenko, R. Yang, R. V. Gorbachev, P. Blake, A. S. Mayorov, K. S. Novoselov, M. I. Katsnelson, and A. K. Geim. Density of states and zero Landau level probed through capacitance of graphene. *Phys. Rev. Lett.*, 105(13):136801, Sep 2010.

[63] Cheol-Hwan Park, Feliciano Giustino, Marvin L. Cohen, and Steven G. Louie. Velocity renormalization and carrier lifetime in graphene from the electron-phonon interaction. *Phys. Rev. Lett.*, 99:086804, Aug 2007.

[64] C.H. Park, F. Giustino, M.L. Cohen, and S.G. Louie. Electron- phonon interactions in graphene, bilayer graphene, and graphite. *Nano letters*, 8(12):4229–4233, 2008.

[65] Jia-An Yan, W. Y. Ruan, and M. Y. Chou. Electron-phonon interactions for optical-phonon modes in few-layer graphene: First-principles calculations. *Phys. Rev. B*, 79:115443, Mar 2009.

[66] J. Gonzalez, F. Guinea, and MAH Vozmediano. Marginal-Fermi-liquid behavior from two-dimensional Coulomb interaction. *Physical Review B*, 59(4):2474–2477, 1999.

[67] X. Du, I. Skachko, F. Duerr, A. Luican, and E.Y. Andrei. Fractional quantum Hall effect and insulating phase of Dirac electrons in graphene. *Nature*, 462(7270):192–195, 2009.

[68] K.I. Bolotin, F. Ghahari, M.D. Shulman, H.L. Stormer, and P. Kim. Observation of the fractional quantum Hall effect in graphene. *Nature*, 462(7270):196–199, 2009.

[69] Y.J. Song, A.F. Otte, Y. Kuk, Y. Hu, D.B. Torrance, et al. High-resolution tunnelling spectroscopy of a graphene quartet. *Nature*, 467(7312):185–189, 2010.

[70] X. Du, I. Skachko, A. Barker, and E.Y. Andrei. Approaching ballistic transport in suspended graphene. *Nature Nanotechnology*, 3(8):491–495, 2008.

[71] K.I. Bolotin, K.J. Sikes, Z. Jiang, M. Klima, G. Fudenberg, J. Hone, P. Kim, and H.L. Stormer. Ultrahigh electron mobility in suspended graphene. *Solid State Communications*, 146(9-10):351–355, 2008.

[72] P. Balk. The Si-SiO$_2$ system. *Materials science monographs*, 32, 1988.

[73] Y.B. Park and S.W. Rhee. Microstructure and interfacial states of silicon dioxide film grown by low temperature remote plasma enhanced chemical vapor deposition. *Journal of Applied Physics*, 86:1346, 1999.

[74] Y.B. Park and S.W. Rhee. Effects of chlorine addition on the silicon dioxide properties deposited with remote plasma enhanced chemical vapor deposition at low temperatures. *Applied Physics Letters*, 66:3477, 1995.

[75] J.C. Alonso, A. Ortiz, and C. Falcony. Low temperature sio2 films deposited by plasma enhanced techniques. *Vacuum*, 43(8):843–847, 1992.

[76] T. Ando and Y. Uemura. Theory of quantum transport in a two-dimensional electron system under magnetic fields. i. characteristics of level broadening and transport under strong fields. *Journal of the Physical Society of Japan*, 36:959, 1974.

[77] N. M. R. Peres, F. Guinea, and A. H. Castro Neto. Electronic properties of disordered two-dimensional carbon. *Phys. Rev. B*, 73:125411, Mar 2006.

[78] W. Zhu, Q. W. Shi, X. R. Wang, J. Chen, J. L. Yang, and J. G. Hou. Shape of disorder-broadened Landau subbands in graphene. *Phys. Rev. Lett.*, 102:056803, Feb 2009.

[79] O.E. Dial, R.C. Ashoori, L.N. Pfeiffer, and K.W. West. High-resolution spectroscopy of two-dimensional electron systems. *Nature*, 448(7150):176–179, 2007.

[80] M. Polini, R. Asgari, Y. Barlas, T. Pereg-Barnea, and A.H. MacDonald. Graphene: A pseudochiral Fermi liquid. *Solid State Communications*, 143(1-2):58–62, 2007.

[81] D. C. Elias, R. V. Gorbachev, A. S. Mayorov, S. V. Morozov, A. A. Zukov, P. Blake, L.A. Ponomarenko, Grigorieva I.V., K. S. Novolselov, A. K. Geim, and F. Guinea. Dirac cones reshaped by interaction effects in suspended graphene. *Nature Physics*, (7):701–704, 2011.

[82] A. Luican, G. Li, E.Y. Andrei, et al. Visualizing the effect of isolated Coulomb impurities in the quantum Hall regime in graphene. *in preparation*.

[83] K. v. Klitzing, G. Dorda, and M. Pepper. New method for high-accuracy determination of the fine-structure constant based on quantized hall resistance. *Phys. Rev. Lett.*, 45:494–497, Aug 1980.

[84] D.L. Miller, K.D. Kubista, G.M. Rutter, M. Ruan, W.A. de Heer, M. Kindermann, et al. Real-space mapping of magnetically quantized graphene states. *Nature Physics*, 6(10):811–817, 2010.

[85] G. Li, A. Luican, and E.Y. Andrei. Self-navigation of a scanning tunneling microscope tip toward a micron-sized graphene sample. *Review of Scientific Instruments*, 82:073701, 2011.

[86] G. Li, A. Luican-Mayer, D. Abanin, L. Levitov, and E.Y. Andrei. Evolution of Landau levels into edge states in graphene. *Nature Communications*, 4, 2013.

[87] Li Yang, Cheol-Hwan Park, Young-Woo Son, Marvin L. Cohen, and Steven G. Louie. Quasiparticle energies and band gaps in graphene nanoribbons. *Phys. Rev. Lett.*, 99:186801, Nov 2007.

[88] Y.W. Son, M.L. Cohen, and S.G. Louie. Energy gaps in graphene nanoribbons. *Physical Review Letters*, 97(21):216803, 2006.

[89] Ç.Ö. Girit, J.C. Meyer, R. Erni, M.D. Rossell, C. Kisielowski, L. Yang, C.H. Park, M.F. Crommie, M.L. Cohen, S.G. Louie, et al. Graphene at the edge: stability and dynamics. *Science*, 323(5922):1705, 2009.

[90] M. Fujita, K. Wakabayashi, K. Nakada, and K. Kusakabe. Peculiar localized state at zigzag graphite edge. *Journal of the Physical Society of Japan*, 65(7):1920–1923, 1996.

[91] Y. Niimi, T. Matsui, H. Kambara, K. Tagami, M. Tsukada, and H. Fukuyama. Scanning tunneling microscopy and spectroscopy of the electronic local density of states of graphite surfaces near monoatomic step edges. *Physical Review B*, 73(8):085421, 2006.

[92] C. Tao, L. Jiao, O.V. Yazyev, Y.C. Chen, J. Feng, X. Zhang, R.B. Capaz, J.M. Tour, A. Zettl, S.G. Louie, et al. Spatially resolving edge states of chiral graphene nanoribbons. *Nature Physics*, 7:616–620, 2011.

[93] D.A. Abanin, P.A. Lee, and L.S. Levitov. Charge and spin transport at the quantum Hall edge of graphene. *Solid state communications*, 143(1-2):77–85, 2007.

[94] D.A. Abanin, P.A. Lee, and L.S. Levitov. Spin-filtered edge states and quantum Hall effect in graphene. *Physical Review Letters*, 96(17):176803, 2006.

[95] V.M. Pereira and A.H. Castro Neto. Strain engineering of graphene electronic structure. *Physical Review Letters*, 103(4):46801, 2009.

[96] F. Guinea, M.I. Katsnelson, and A.K. Geim. Energy gaps and a zero-field quantum Hall effect in graphene by strain engineering. *Nature Physics*, 6(1):30–33, 2009.

[97] Edward McCann. Asymmetry gap in the electronic band structure of bilayer graphene. *Phys. Rev. B*, 74:161403, Oct 2006.

[98] F. Guinea, A. H. Castro Neto, and N. M. R. Peres. Electronic states and Landau levels in graphene stacks. *Phys. Rev. B*, 73:245426, Jun 2006.

[99] Y. Zhang, T.T. Tang, C. Girit, Z. Hao, M.C. Martin, A. Zettl, M.F. Crommie, Y.R. Shen, and F. Wang. Direct observation of a widely tunable bandgap in bilayer graphene. *Nature*, 459(7248):820–823, 2009.

[100] R. T. Weitz, M. T. Allen, B. E. Feldman, J. Martin, and A. Yacoby. Broken-symmetry states in doubly gated suspended bilayer graphene. *Science*, 330(6005):812–816, 2010.

[101] A. S. Mayorov, D. C. Elias, M. Mucha-Kruczynski, R. V. Gorbachev, T. Tudorovskiy, A. Zhukov, S. V. Morozov, M. I. Katsnelson, V. I. Falko, A. K. Geim, and K. S. Novoselov. Interaction-driven spectrum reconstruction in bilayer graphene. *Science*, 333(6044):860–863, 2011.

[102] B.E. Feldman, J. Martin, and A. Yacoby. Broken-symmetry states and divergent resistance in suspended bilayer graphene. *Nature Physics*, 5(12):889–893, 2009.

[103] A. Deshpande, W. Bao, Z. Zhao, C.N. Lau, and BJ LeRoy. Mapping the Dirac point in gated bilayer graphene. *Applied Physics Letters*, 95:243502, 2009.

[104] G.M. Rutter, S. Jung, N.N. Klimov, D.B. Newell, N.B. Zhitenev, and J.A. Stroscio. Microscopic polarization in bilayer graphene. *Nature Physics*, (7):649–655, 2011.

[105] Z. Y. Rong and P. Kuiper. Electronic effects in scanning tunneling microscopy: Moiré pattern on a graphite surface. *Phys. Rev. B*, 48:17427–17431, Dec 1993.

[106] J. Xhie, K. Sattler, M. Ge, and N. Venkateswaran. Giant and supergiant lattices on graphite. *Phys. Rev. B*, 47:15835–15841, Jun 1993.

[107] K. Kobayashi. Moiré pattern in scanning tunneling microscopy of monolayer graphite. *Phys. Rev. B*, 50:4749–4755, Aug 1994.

[108] W.T. Pong and C. Durkan. A review and outlook for an anomaly of scanning tunnelling microscopy (STM): superlattices on graphite. *Journal of Physics D: Applied Physics*, 38:R329, 2005.

[109] J. M. B. Lopes dos Santos, N. M. R. Peres, and A. H. Castro Neto. Graphene bilayer with a twist: Electronic structure. *Phys. Rev. Lett.*, 99:256802, Dec 2007.

[110] G. Trambly de Laissardie're, D. Mayou, and L. Magaud. Localization of dirac electrons in rotated graphene bilayers. *Nano Letters*, 10(3):804–808, 2010.

[111] E. J. Mele. Commensuration and interlayer coherence in twisted bilayer graphene. *Phys. Rev. B*, 81:161405, Apr 2010.

[112] Rafi Bistritzer and Allan H. MacDonald. Moiré bands in twisted double-layer graphene. *Proceedings of the National Academy of Sciences*, 108(30):12233–12237, 2011.

[113] S. Shallcross, S. Sharma, E. Kandelaki, and O. A. Pankratov. Electronic structure of turbostratic graphene. *Phys. Rev. B*, 81:165105, Apr 2010.

[114] S. Shallcross, S. Sharma, and O. A. Pankratov. Quantum interference at the twist boundary in graphene. *Phys. Rev. Lett.*, 101:056803, Aug 2008.

[115] A. Luican, Guohong Li, A. Reina, J. Kong, R. R. Nair, K. S. Novoselov, A. K. Geim, and E. Y. Andrei. Single-layer behavior and its breakdown in twisted graphene layers. *Phys. Rev. Lett.*, 106:126802, Mar 2011.

[116] L. Van Hove. The occurrence of singularities in the elastic frequency distribution of a crystal. *Physical Review*, 89(6):1189, 1953.

[117] M. Fleck, A. M. Oleś, and L. Hedin. Magnetic phases near the Van Hove singularity in s- and d-band Hubbard models. *Phys. Rev. B*, 56:3159–3166, Aug 1997.

[118] J. González. Kohn-Luttinger superconductivity in graphene. *Phys. Rev. B*, 78:205431, Nov 2008.

[119] T. M. Rice and G. K. Scott. New mechanism for a charge-density-wave instability. *Phys. Rev. Lett.*, 35:120–123, Jul 1975.

[120] J. Hicks, M. Sprinkle, K. Shepperd, F. Wang, A. Tejeda, A. Taleb-Ibrahimi, F. Bertran, P. Le Fèvre, W. A. de Heer, C. Berger, and E. H. Conrad. Symmetry breaking in commensurate graphene rotational stacking: Comparison of theory and experiment. *Phys. Rev. B*, 83:205403, May 2011.

[121] D. L. Miller, K. D. Kubista, G. M. Rutter, M. Ruan, W. A. de Heer, P. N. First, and J. A. Stroscio. Structural analysis of multilayer graphene via atomic Moiré interferometry. *Phys. Rev. B*, 81:125427, Mar 2010.